Journal of
Composites Science

MDPI

Article

Characterization of Electrospun PAN Polymer Nanocomposite Membranes for CO_2/N_2 Separation

Dirar Aletan and Jacob Muthu *

Faculty of Engineering and Applied Science, University of Regina, 3737 Wascana Parkway, Regina, SK S4S 0A2, Canada; dac276@uregina.ca
* Correspondence: jacob.muthu@uregina.ca; Tel.: +1-306-337-8125

Abstract: The focus of this study was to enhance the CO_2 capture capabilities of polyacrylonitrile (PAN) nanocomposite membranes by reinforcing them with multi-walled carbon nanotubes (MWCNT) and silica (SiO_2). These nanocomposite membranes were created using electrospinning technology, which produced nonwoven nanofiber membranes. The nanoparticles were functionalized using Gum Arabic (GA) to improve the distribution and prevent agglomeration. Fourier transform infrared (FTIR) and scanning electron microscopy (SEM) analysis were conducted to examine the functionalization of nanoparticles and their morphological structures. The membranes were experimentally characterized to obtain the CO_2 absorption properties and also to evaluate CO_2/N_2 permeation properties compared to pure PAN membranes. The results showed that higher nanoparticle concentrations increased CO_2 permeability while maintaining stable N_2 permeability, ensuring favorable CO_2/N_2 selectivity ratios. The 4 wt.% MWCNTs nanocomposite membrane achieved the best CO_2/N_2 separation with a CO_2 permeability of 289.4 Barrer and a selectivity of 6.3, while the 7 wt.% SiO_2 nanocomposite membrane reached a CO_2 permeability of 325 Barrer and a selectivity of 7. These findings indicate significant improvements in CO_2 permeability and selectivity for the nanocomposite membranes compared to pure PAN membranes. The Maxwell mathematical model has been used to validate the experimental results. The experimental results of the CO_2 separation properties of the nanocomposite membranes exceeded the predicted values by the mathematical models. This might be due to the well-dispersed nanoparticles and functional groups.

Keywords: electrospinning; nanocomposite membranes; CO_2 separation; permeability and selectivity; PAN polymer; MWCNTs and SiO_2 nanoparticles

check for updates

Academic Editor: Mazeyar Parvinzadeh Gashti

Received: 23 November 2024
Revised: 30 December 2024
Accepted: 3 January 2025
Published: 6 January 2025

Citation: Aletan, D.; Muthu, J. Characterization of Electrospun PAN Polymer Nanocomposite Membranes for CO_2/N_2 Separation. *J. Compos. Sci.* **2025**, *9*, 21. https://doi.org/10.3390/jcs9010021

Copyright: © 2025 by the authors. Licensee MDPI, Basel, Switzerland. This article is an open access article distributed under the terms and conditions of the Creative Commons Attribution (CC BY) license (https://creativecommons.org/licenses/by/4.0/).

1. Introduction

The consequences of fossil fuel consumption for the ever-increasing energy demand led to increased greenhouse gas (GHG) emissions, resulting in aggressive environmental disasters, including climate change, more health risks, rising oceans, and the loss of natural habitat [1–3]. Since carbon dioxide (CO_2) emissions are the main contributors to GHG emissions [4], government agencies, research centers, and industries are actively working on finding new ways to mitigate CO_2 emissions. This has led to carbon capture and storage (CCS) becoming a leading pathway for damping carbon dioxide emissions. Various methods are used for CCS, among which chemical and physical absorption and membrane separation dominate the CO_2-capturing process [5].

Chemical absorption techniques have been commercially popular due to technological advancements and development for many years. The amine-based solvents are mostly

preferred for chemical absorption due to their high reactivity and commercial availability. However, these solvents lose their performance over time mainly due to degeneration and volatility, increasing corrosion [6]. Moreover, the modest CO_2 partial pressure in flue gases produces less driving force of CO_2 absorption from gas streams, which results in energy exhaustion during capture and solvent regeneration [7]. The physical absorption techniques use physical solvents such as dimethyl ethers of poly (ethylene glycol) (DEPG) [8] under high feed pressure to absorb CO_2 when the other gasses within a gas mixture have relatively small solubility. In this process, no chemical reactions lead to no chemical wastes and have a high potential for large industrial scale. However, the major downside of physical absorption solvents is the high energy costs due to the additional heat transfer requirements for solvent regeneration [5].

On the other hand, physical gas separation using membranes has shown more significant potential to tackle the challenges associated with both chemical and physical absorption techniques. With moderate energy requirements, lesser chemical interaction resulting in negligible corrosion over time, simple operation procedures, and easy maintenance [9], membrane separations have an edge over the absorption process. Generally, membranes are manufactured using inorganic or organic materials. Inorganic membranes made from ceramic and metallic materials, as well as zeolite, are selected for their high-pressure and temperature durability [10]. However, their brittle nature, limited scalability, and resource cost are a significant challenge for the industrial-scale CO_2 separation process.

Organic membranes are mainly made from natural or synthetic polymers. Polymers are categorized based on crystallinity to crystalline, semi-crystalline, and amorphous [11]. Crystalline polymers are not favorable materials for manufacturing membranes due to their orderly structure and low permeability. As such, amorphous and semi-crystalline polymers are generally preferred because of higher gas permeability and better separation performance due to their less ordered structure [12]. Semi-crystalline polymers are generally preferred for CO_2 separation membranes due to better thermal stability, good chemical resistance, and tailored properties [13].

Examples of organic membrane polymers are polyamide (PA), polyethylene (PE), and polyacrylonitrile (PAN), which are used for membrane separation due to their versatile chemical structure and tailored chain packing density [14]. This provides increased CO_2 solubility and faster diffusion rates across the membrane matrix, respectively [15,16]. Other properties, such as inherited micro-porosity [17], thermally rearranged polymers [18], and polymer hybridization [13] made the polymer membrane attractive for gas separation. However, the inferior mechanical strength, which affects the membrane durability, lower resistance to corrosion that impacts the membrane performance under a corrosive environment, and poor thermal stability at high temperatures have hindered the application of polymers for CO_2 separation [19]. Moreover, a trade-off challenge linking permeability and selectivity exists because of the high permeability of polymer membranes, which has limited the CO_2 separation efficiency from other gases [20]. These limitations have led researchers to search for polymer membranes with improved CO_2 permeability and selectivity trade-off (i.e., improved separation performance). The chemical structure of polymers can be modified by many methods while keeping a reasonable permeability and selectivity trade-off, thus encouraging researchers to focus on studying polymer modifications for improved CO_2 separation performance.

Based on the solution–diffusion process, the smaller gas molecules (e.g., CO_2) are adsorbed, then diffused across the membrane matrix, and eventually desorbed after the diffusion process [9], while the larger gas molecules (e.g., N_2) retentate. This defines membrane performance as permeability and selectivity. As such, permeability can be described as the capacity of a membrane to permit gas molecules to permeate through them

by diffusion mechanism. The gas selectivity of a membrane is the permeability ratio of a more permeable gas to a lower permeable gas, which indicates the membrane's effectiveness in separating different gases. Further, the penetrated gas is adsorbed/absorbed onto the membrane and then diffused throughout, before desorbing into the permeate membrane side [21]. As such, diffusivity refers to the rate at which gas diffuses across a membrane based on gas molecular size, the membrane morphology, and the compatibility or solubility limit of the gas solute within the membrane matrix. Solubility is the ability of a gas to dissolve in a membrane matrix. However, the higher solubility of a gas in a membrane matrix can enhance its permeability but not necessarily the selectivity. For example, a higher CO_2 permeable membrane will increase other gases' permeability, leading to lower membrane selectivity. Further, the low CO_2 partial pressure directly hinders the membrane gas separation and thus reduces the durability of the membranes. In line with the above discussion, it can be confirmed that the permeability and selectivity trade-off, diffusivity, solubility, and long-term stability are the determinant factors in decoding the effectiveness of the polymer membranes.

On that account, it is pivotal to design novel membrane materials that produce an efficient, durable membrane with improved permeability and selectivity, reasonable trade-off performance, and enhanced solubility and diffusivity for extracting relatively low CO_2 concentrations from flue gases. This has resulted in the researchers focusing on functionally modifying polymer membranes using nano-reinforcements to optimize the membrane performance for CO_2 capture. The polymers were modified by incorporating nanoparticles, thus creating novel polymer nanocomposite membranes [22]. The size, shape, and weight fractions of nanoparticles, as well as functionalization additives, are major variables that affect the effectiveness of the nanocomposite membranes for CO_2 separation [23,24]. The research results showed that infusing nanoparticles can modify the characteristics of a membrane, resulting in improved thermal stability, increased contact surface area, free volumes, and gas pathways, promoting the permeability and selectivity of the polymeric membranes [5,25]. Tseng et al. [24] analyzed the effect of infusing multi-walled carbon nanotubes (MWCNT) into an amorphous Polyimide (PI) matrix for CO_2/N_2 separation. The MWCNT-reinforced PI nanocomposite membrane improved the CO_2 permeability of the PI membrane from about 223 to 867 Barrer. Also, the MWCNT/PI showed an improved CO_2/N_2 selectivity of 4.1, which is twice greater than the pure PI membrane. This improvement was accredited to the ultra-smooth surface of the MWCNTs, which resulted in negligible friction for gas molecules that prompted increased gas transport pathways [26,27]. Hu et al. [28] infused 20 wt.% of silica (SiO_2) nanoparticles with an amorphous PI matrix, developing a SiO_2/PI nanocomposite membrane, which showed a CO_2 permeability of 210 Barrer and a selectivity of 30.8, respectively. The reasons behind the improved CO_2 permeability are the increased CO_2 solubility, diffusivity, free volume, and upgraded transport pathways in the PI membrane through the addition of SiO_2 nanoparticles. The infusing of 20 wt.% of SiO_2 improved the solubility of the pure PI membrane from 6.6 to 7.6 (10^{-2} cm^3 (STP)/cm^3 cmHg) and the diffusivity from 10.1 to 27.6 (10^{-8} cm^2/s), respectively. The significant increase in solubility and diffusivity directly affected the permeability improvement. However, the increased free volume and transport pathways increased the permeation of other gases, affecting the selectivity of the membranes. Jiang et al. [13] infused MWCNT nanoparticles into polyether-block-polyamide (Pebax-1074) polymer to prepare MWCNT/Pebax nanocomposite membranes for CO_2/N_2 separation. The infusing of 12 wt.% MWCNTs altered the microstructure of the prepared nanocomposite membrane, which improved the gas separation properties, thus raising the CO_2 permeability to 291.4 Barrer and the selectivity to 160.2, respectively. Moreover, Khalilinejad et al. [29] developed a SiO_2/Pebax polymer nanocomposite membrane to

characterize the performance of CO_2/N_2 separation. Compared to pure Pebax, the results showed that adding 8 wt.% of SiO_2 has improved the CO_2 permeability and selectivity of the SiO_2/Pebax nanocomposite membrane to 124 Barrer and 76, respectively. In addition, the CO_2 solubility has increased from about 50 to 129 (10^{-4} cm^3 (STP)/cm^3 cmHg) with no significant change in diffusivity. This suggests that CO_2 solubility was vital in improving the CO_2/N_2 separation of the SiO_2/Pebax synthesized membrane.

Though the infusing of nanoparticles has raised the effectiveness of CO_2 separation membranes, the higher demand for a reasonable trade-off between permeability and selectivity accelerates the need for extensive research focusing on the various combinations of polymer nanocomposite to make a valid decision to use these membranes for CO_2 capture. Additionally, transitioning from the current chemical solvent process to the more environment-friendly membrane separation process necessitates the development of more efficient membranes. Therefore, more extensive studies are essential to enhance and optimize the permeability, selectivity, and long-term stability, along with the improved diffusivity and solubility of novel polymer nanocomposite membranes.

Based on the mentioned observations, the objective of this paper was defined as the design and characterization of polyacrylonitrile (PAN) polymer reinforced with multi-walled carbon nanotubes (MWCNTs) and silicon dioxide (SiO_2) nanocomposite membranes. The PAN polymer was selected as a membrane matrix due to several advantages, such as high CO_2 selectivity, durability, resistance to both chemical and corrosive environments during operation, cost-effectiveness, and recyclability, with it being environmentally benign [30,31]. The selected nanoparticles were functionalized using Gum Arabic (GA), a biodegradable polymer, before doping with PAN polymer to produce the nanocomposite membrane. The green functionalization improved the nanoparticles' dispersion and the nanocomposite membranes' permeability, selectivity, solubility, and diffusivity. Further, a versatile electrospinning technique was designed to produce the PAN and the nanocomposite membranes. The spinning technique was selected due to its ease of operation in doping the nanoparticles with the PAN polymer matrix, which further enabled them to produce controlled selective nanocomposite layers within the membrane. Finally, the membranes were experimentally characterized using the in-house permeation test facility to characterize the effect of nano-reinforcements on the permeability, selectivity, diffusivity, and solubility of the PAN nanocomposite membrane. The experimental results were then validated using Maxwell's mathematical modeling.

2. Materials and Methods

2.1. Materials

Polyacrylonitrile (PAN) polymer and the nano-reinforcements (MWCNT and SiO_2) were purchased from Sigma Aldrich, Canada. The MWCNT particles have diameters of 6–13 nm and lengths of 2.5–20 μm, with a purity greater than 98%. The spherical SiO_2 particles have a 10–20 nm diameter, with 99.5% purity. The Gum Arabic (GA) polymer was purchased from Millipore Sigma, USA, for functionalization. Since the flue gas compositions are 87% N_2 and 13% CO_2, only CO_2 and N_2 were selected for separation analysis. The gas cylinders were purchased from Linde Inc., Canada, to characterize the performance of the synthesized membrane. The N-dimethylformamide (DMF) (99% purity) solvent and other laboratory-grade reagents were used during experiments.

2.2. Morphological Characterization

The morphological characterization of pure PAN and its nanocomposite membranes was performed using SEM (Hitachi UHR FE-SEM SU8000) at 5–30 KV. Specimens were coated with carbon and Au/Pd via an EMITECH K950X evaporator and K550X sputter

coater and fixed with DAG 580 colloidal graphite. FTIR analysis was performed with a Thermo Scientific Nicolet iS20 IR spectrometer using a Smart iTX accessory with a Diamond Crystal cell in the ATR setting, taking 32 scans per sample at 4 cm^{-1} resolution. TGA and DTG analyses, using TA-60 Model Shimadzu Instruments, measured the thermal stability of PAN nanocomposite membranes across 20–800 °C at a 30 °C/min heating rate in nitrogen, characterizing their thermodynamic nature.

2.3. Functionalization of Nanoparticles

The selected nano-reinforcements were functionalized using Gum Arabic (GA) to improve the dispersion and adhesion with the PAN polymer. The functionalization process was started by mixing 0.1 molar Sodium Chloride (NaCl) solution with 10 weight percent (wt.%) of Gum Arabic at 60 °C for 6 h. Afterward, the required (wt.%) of nanoparticles were added and stirred at 60 °C for 12 h, followed by 5 min of sonication. Next, the resulting solution was centrifuged for two hours at 3000 rpm to separate the finer aggregates. Finally, a filtration and drying process was used to produce the functionalized nanoparticles, which were doped with the PAN polymer matrix, using an electrospinning setup to produce polymer nanocomposite membranes.

Figure 1a illustrates the ATR-FTIR analysis results of both unfunctionalized and GA-functionalized MWCNT. The FTIR spectrum of the functionalized MWCNT shows an OH functional group due to GA functionalization at the 3245 peak, which is due to the alcohol or phenol group [32]. Moreover, the peaks at 2897 cm^{-1} and 1766 cm^{-1} are due to C-H stretching and C-C stretching, respectively. The peak at 1596 cm^{-1} of N-H stretching is due to the 1° amines, while the C-N stretch vibration at 1257 cm^{-1} could be due to an aliphatic amine. The acute peak at 1001 cm^{-1} could be due to the C-H bend of alkenes [32] or the 5- and 6-member rings in the monosaccharides found in GA [33]. The GA functionalization leads to protective layers around the MWCNTs created by polysaccharide and glycoprotein macro-molecules in GA, which prevents agglomeration. Further, the functionalization creates electrostatic layers due to the reaction between free electrons in the π (P_z) orbitals of C=C bonds in MWCNT nanoparticles and various functional groups in the polysaccharides. This reaction significantly improves the dispersion stability of the functionalized MWCNTs (GA-MWCNTs), thereby improving their gas separation performance.

Similarly, the functionalized SiO_2 was also analyzed using FTIR, as shown in Figure 1b. The spectrum results of functionalized SiO_2 show an OH functional group at 3354 cm^{-1} due to the alcohol or phenol group in GA [33]. Moreover, the peaks at 2983 cm^{-1} are related to C-H stretching. The peak at 2168 cm^{-1} corresponds to the C-C stretching. The peak at 1610 cm^{-1} corresponds to the N-H stretching due to 1° amines. The peak at 1416 cm^{-1} of the C-H vibrations is due to alkanes, and the peak at 539 cm^{-1} correlates to the C-I stretch due to alkyl halides. The attached functional group improves the dispersion stability of SiO_2 within the PAN polymer, which is expected to improve the gas separation. Moreover, the functionalization of nanoparticles using Gum Arabic is expected to upgrade nanocomposite membranes by improving the corrosion resistance, stability, surface properties, and hydrophilicity of synthesized nanoparticles, ultimately benefiting CO_2 separation processes. Gum Arabic could serve as a reducing agent, modifying the surface of NPs and preventing their aggregation, with which the properties of nanocomposite membranes can be tailored for CO_2 separation [33].

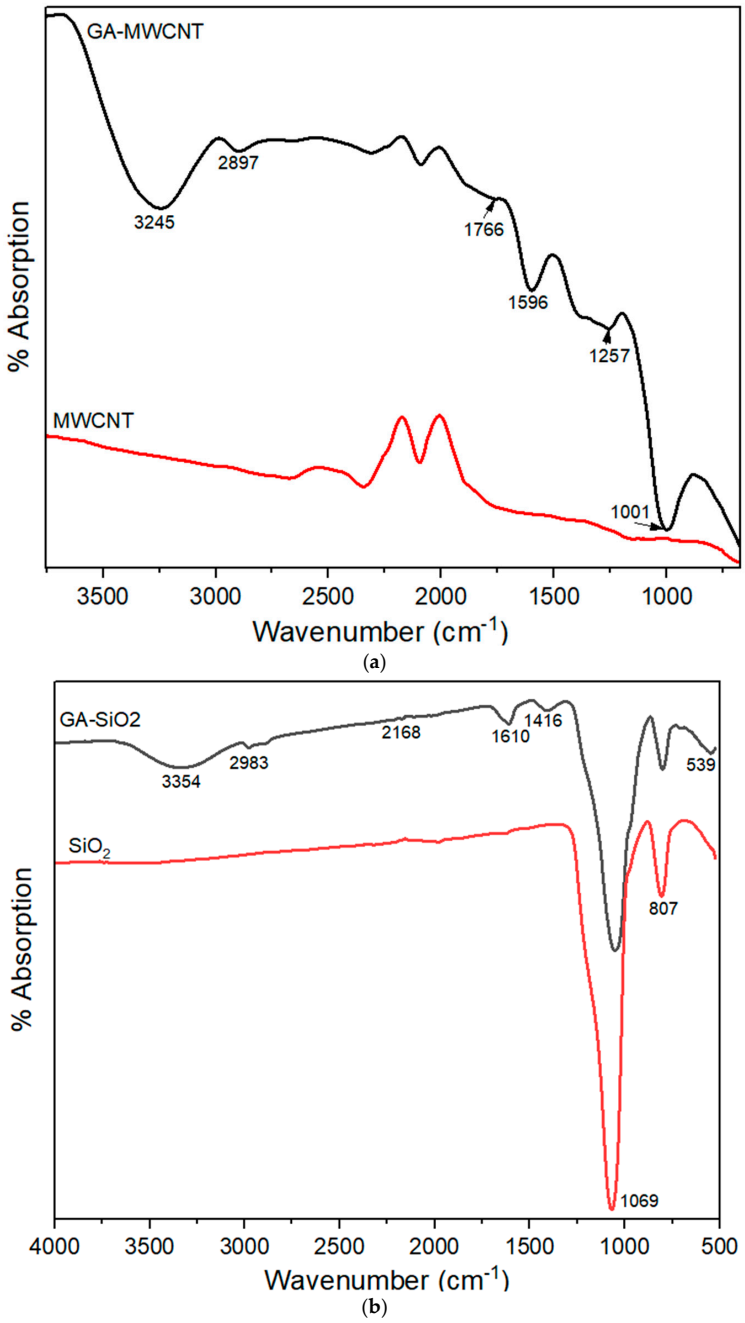


Figure 1. (**a**) ATR-FTIR spectrum of unfunctionalized MWCNT and GA-functionalized MWCNT; (**b**) ATR-FTIR spectrum of pristine SiO_2 and GA-functionalized SiO_2.

2.4. Design and Development of Electrospinning Facility

An electrospinning setup for manufacturing doped nanofiber membranes was designed and developed. The electrospinning assembly consists of a DC voltage power supply of 50 kV max capabilities (Gamma High Voltage and Research, Florida, USA), a NE-1600 syringe pump from New Era Pump Systems Inc., New York, USA, and a grounded rotating collector drum to collect a substantial mass of continuous fibers (MTI Corporations, California, USA). These individual pieces of equipment were assembled to set up the electrospinning facility. Once the final design required for producing doped continuous nanofibers was ready, the electrospinning of pure PAN and PAN nanocomposite membranes was carried out.

Before manufacturing the nanocomposite membrane, the solution and the operation parameters were analyzed to produce smooth, uniform nanofibers. The specifications of the

electrospinning solution, including polymer weight fractions, viscosity, and conductivity, were critical in determining fiber morphology. Viscosity was analyzed by varying PAN concentrations from 2 to 10 g in DMF solution. No nanofibers formed at 1–2 g, leading to electrospraying. At 2–4 g, inconsistent nanofibers and beads were produced. Suitable PAN concentrations (4–8 g) yielded smooth, uniform nanofibers (refer to Figure 2a), while 8–10 g resulted in rough, distorted fibers (refer to Figure 2b).

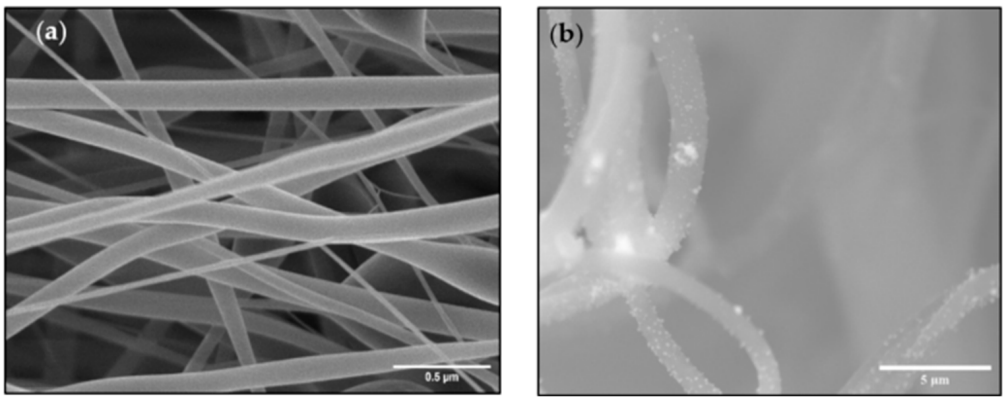


Figure 2. Electrospun nanofiber with varying operation and solution parameters: (**a**) 4–8 g of electrospun PAN nanofiber membrane; (**b**) 8–10 g of rough, distorted, and pitted fibers.

The needle diameter was set at 18 G with a 90° angled end tip for uniform fiber manufacturing. The flow rate varied between 1 and 2 mL/h, with higher rates resulting in larger diameters and beads. The distance between electrodes ranged from 0 to 25 cm; distances less than 10 cm caused poor surface roughness, while distances over 25 cm led to thinned and broken fibers.

The interlinked solution and operation parameters, such as voltage, distance between electrodes, and polymer weight fractions in the DMF solution, were studied. An electrospinning parameter matrix was created (refer to Figure 3), varying voltage (10–20 kV) and electrode distance (15–20 cm) for different polymer weight fractions (4, 6, 8 g). The optimal parameters were 6 g PAN in DMF, 15 kV, and 15 cm. Afterwards, using these optimum electrospinning parameters, 4, 6, and 8 g of PAN, producing different fiber densities of pure PAN membrane, were selected to analyze the effect of PAN weight loadings on CO_2 capture.

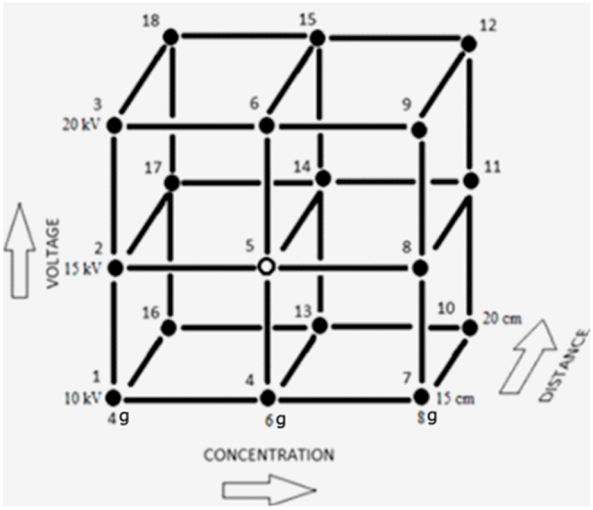


Figure 3. Electrospinning parameter matrix.

2.5. Electrospinning Procedure

After determining the optimum electrospinning parameters, PAN and PAN nanocomposite membranes were produced. Before spinning, the required PAN was mixed with DMF solutions. The syringe pump flow rate was set between 1 and 2 mL/hr. Electrodes were secured, and the collector motor speed was adjusted. A DC voltage supply of 15 KV was used. Post electrospinning, the PAN membrane was cured in a laboratory oven to stabilize porosity, provide structural stability, and remove solvents and impurities [34,35]. A similar procedure was used for nanocomposite membranes, with weight fractions of MWCNT and SiO_2 at 1, 4, 7, and 10 wt.%. Higher MWCNT concentrations (>10 wt.%) reduced solution viscosity, causing electrospraying instead of electrospinning. Further, SiO_2 concentrations >10 wt.% led to the aggregation, clustering, and improper dispersion of nanoparticles [36–39]. Once the weight fractions were finalized, nanocomposite membranes were produced. The selected nanoparticle weight fraction was mixed with DMF at 80 °C for 2 h, followed by sonication for 15 min. The solution was then mixed with PAN-DMF solution and magnetically stirred at 80 °C for 24 h to create NPs/PAN-DMF solutions. The solution was then electrospun to produce nanocomposite membranes and finally cured in the laboratory oven at 60 °C for 24 h to stabilize the membrane's porosity, provide structural stability, and remove solvents.

2.6. CO_2/N_2 Separation Measurements

The nanocomposite membranes were evaluated using a permeation setup, involving a pressure gradient to assess gas permeability under constant volume and room temperature, as per ASTM D1434-82 and ISO 15105-1 standards [40,41]. The setup includes a feed cell and a permeation cell as shown in Figure 4. The pressure gradient at the permeation cell directly relates to gas permeability, as shown in Equation (1).

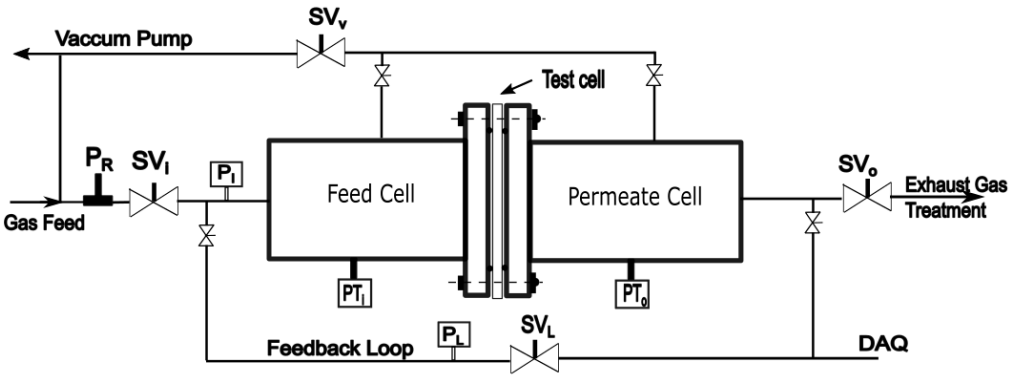


Figure 4. The schematic of the experimental permeation setup.

The setup was controlled by solenoid valves to minimize human interaction. A pressure relief valve (P_R) depressurized the system, while feed pressure (p_f) was regulated and measured by a pressure-temperature transducer (PT_I). The permeation cell was calibrated to a volume of 249.37 cm^3. The gas permeation gradient (dp_i/dt) was monitored by a transducer (PT_O) with a solenoid valve (SV_O) to prevent overpressure. The feedback loop was used to control solenoid valves. The entire setup was vacuumed before testing and was controlled by the valve (SV_v). The data acquisition system (DAQ) controlled and recorded data during testing.

Before testing, the membrane sample was placed between two 0.508 mm polyethylene holders inside a two-plate test cell assembly to prevent gas leaks. The assembled test cell was positioned between the feed and permeate cells, then vacuumed to remove volatile chemicals. The DAQ system, consisting of the NI-9202 module, NI cDAQ-9174 chassis, and

the DAQ Express 5.1 software, acquired signals from pressure–temperature transducers (PT_I and PT_O), converted them to digital data, and used calibration to translate the signals into physical pressure values (cmHg).

Once the test setup was ready, the CO_2 cylinder valve was opened to set a pressure of 1.1 bar and was allowed to flow through the feed cell. Then, the control valve between the cells was opened, to allow for CO_2 to flow from the feed cell to the permeating cell. The pressure and temperature at the feed and permeate cells were monitored and measured by the pressure–temperature transducers. The N_2 gas was tested using a similar procedure. Three CO_2 and N_2 permeation test trials have been conducted for all membrane samples to confirm the repeatability. The acquired data were then used to calculate the permeate cell's pressure gradient (dpi/dt). Further, the acquired data were processed to calculate the measurements of permeability (P) in Barrer, diffusivity (D) in (cm^2/s), solubility (S), and selectivity ($\alpha_{CO2/N2}$).

The permeability of the membrane for both CO_2 and N_2 was calculated using Equation (1), derived from the ideal gas law for permeating gas 'i' [42].

$$P_i = \frac{22,415 \times V_p \times t_m}{p_{i,f} \times R \times T \times A_m} \times \left(\frac{dp_i}{dt}\right) \quad (1)$$

where

- P_i is the permeability of gas (i) in (Barrer) (1 Barrer = 10^{-10} cm^3 (STP) cm/cm^2 s cmHg);
- V_p is the permeate cell volume in (cm^3);
- t_m is the membrane thickness in (cm);
- $p_{i,f}$ is the feed pressure of the gas (i) in (cmHg);
- R is the gas constant in (cm^3 cmHg/gmol K);
- T is the room temperature in (K);
- A_m is the membrane surface area in (cm^2);
- dp_i/dt is the pressure gradient in (cmHg/s);

The diffusivity (D) was calculated from Equation (2) [43].

$$D = \frac{t_m^2}{6\theta} \quad (2)$$

where θ is the time needed for the pressure gradient to reach saturation on the permeation side.

The solubility (S) in (10^{-10} cm^3 (STP)/cm^3 cmHg) was determined using Equation (3) [44].

$$S = \frac{P}{D} \quad (3)$$

Finally, the selectivity (α) of the membranes was calculated using CO_2 permeability (P_{CO2}) to the N_2 permeability (P_{N2}) using Equation (4) [24].

$$\propto_{CO2/N2} = \frac{P_{CO2}}{P_{N2}} \quad (4)$$

3. Results and Discussion

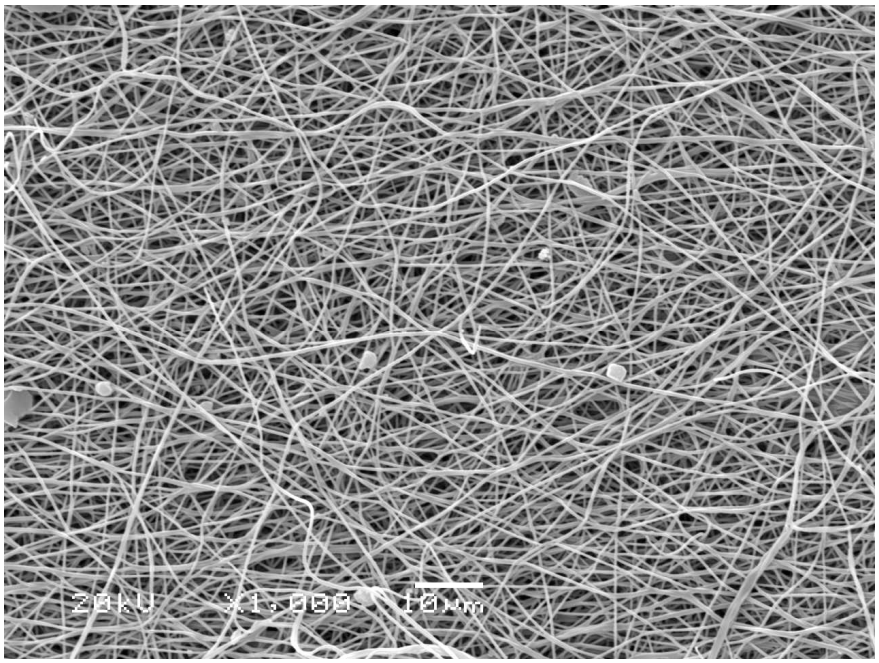
3.1. Structure and Properties of the Membranes

3.1.1. SEM Analysis

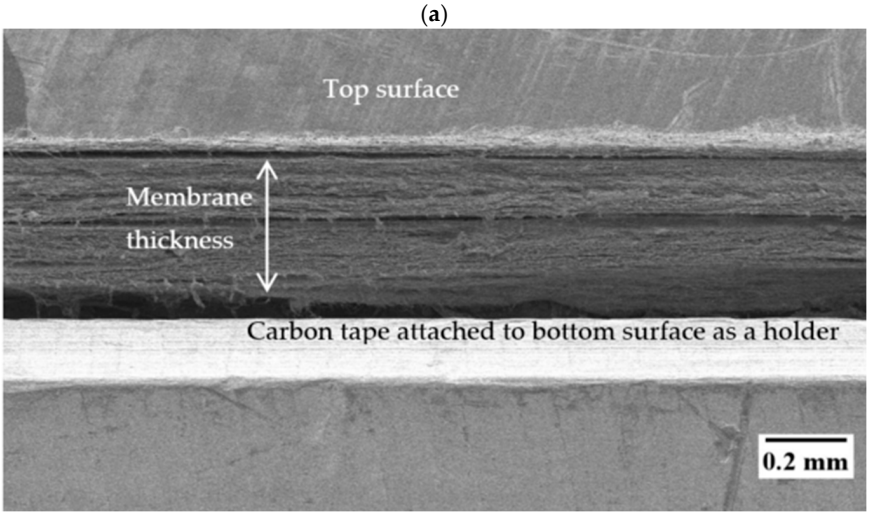
The surface and cross-section morphology of the PAN nanocomposite membranes and the diameter of the nanofibers are shown in Figure 5. Figure 5a,b show the SEM images of the membrane surface morphology and the thickness, respectively. The membrane thickness was between 300 and 420 µm. The diameter of the nanofibers (NFs) was between

100 and 300 nm, as shown in the frequency plots (refer to the Figure 5c–e inserts). The curing of the membrane after spinning has stabilized the nanofibers with smooth surfaces and consistent diameters. Also, it could be observed in the SEM images that the nanofibers are long, cylindrical, and beadless, which confirms that the membranes were produced using the appropriate electrospinning operation and solution parameters.

Figure 5d displays the SEM results of the MWCNT-doped PAN nanofibers, which reveals that the functionalized MWCNTs were homogeneously distributed and aligned along the axis of the PAN nanofibers. According to Ggostsi et al. [45], the alignment of the doped MWCNTs occurs through flow detention and channel-generated alignment in the electrospinning process, which could be possible due to the adhesion of multiple functional groups during functionalization. The alignment of the functionalized MWCNT nanoparticles was expected to facilitate strong interactions of CO_2 molecules, leading to enhanced sorption capacity [46]. Compared with PAN nanofibers, the doping of MWCNTs led to the formation of smoother fibers, and the doping reduced beads and defects, which is anticipated to upgrade the thermal and mechanical stability of the PAN-MWCNT nanocomposite membranes.

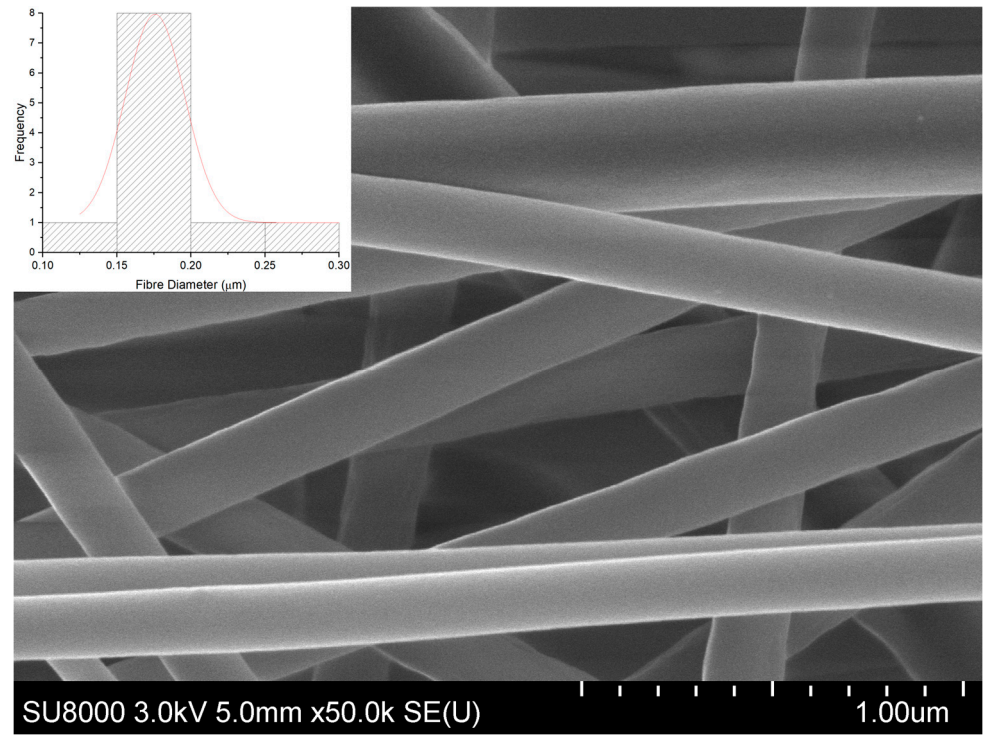


(**a**)

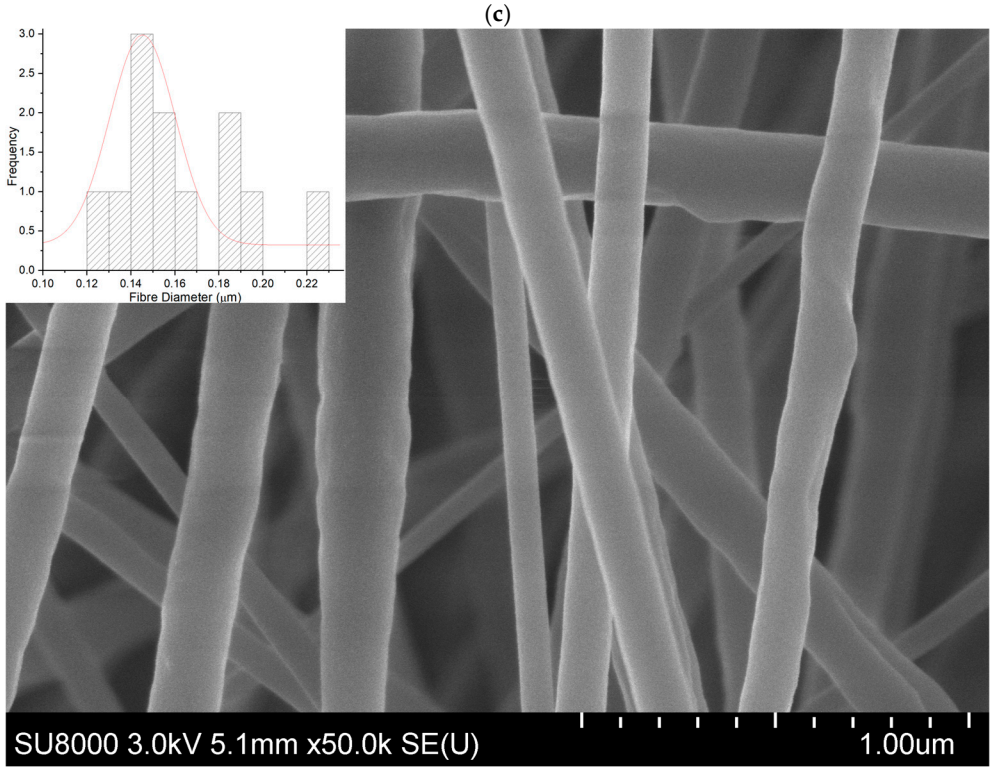


(**b**)

Figure 5. *Cont.*

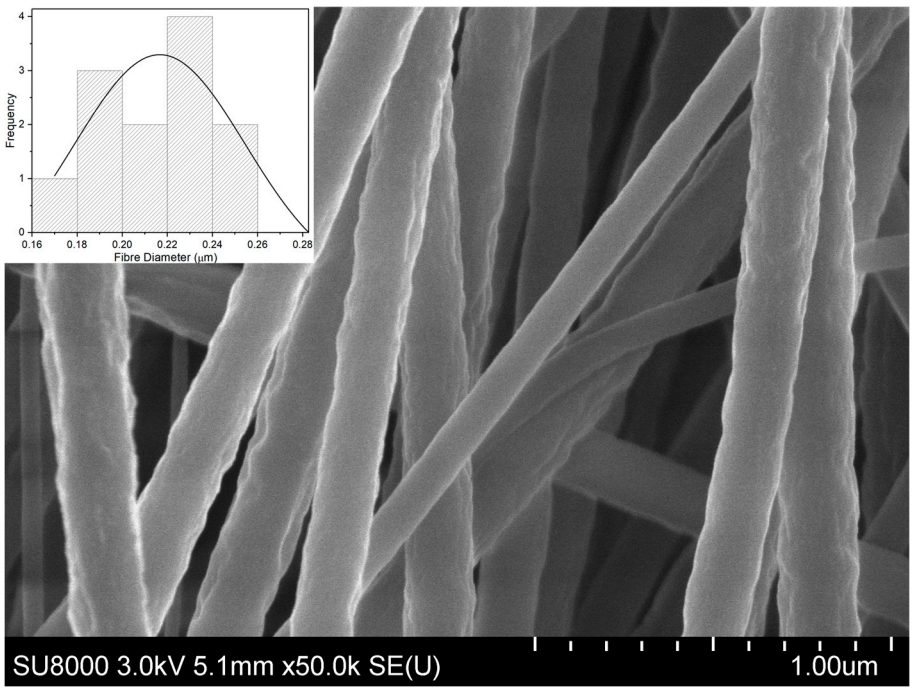


(**c**)

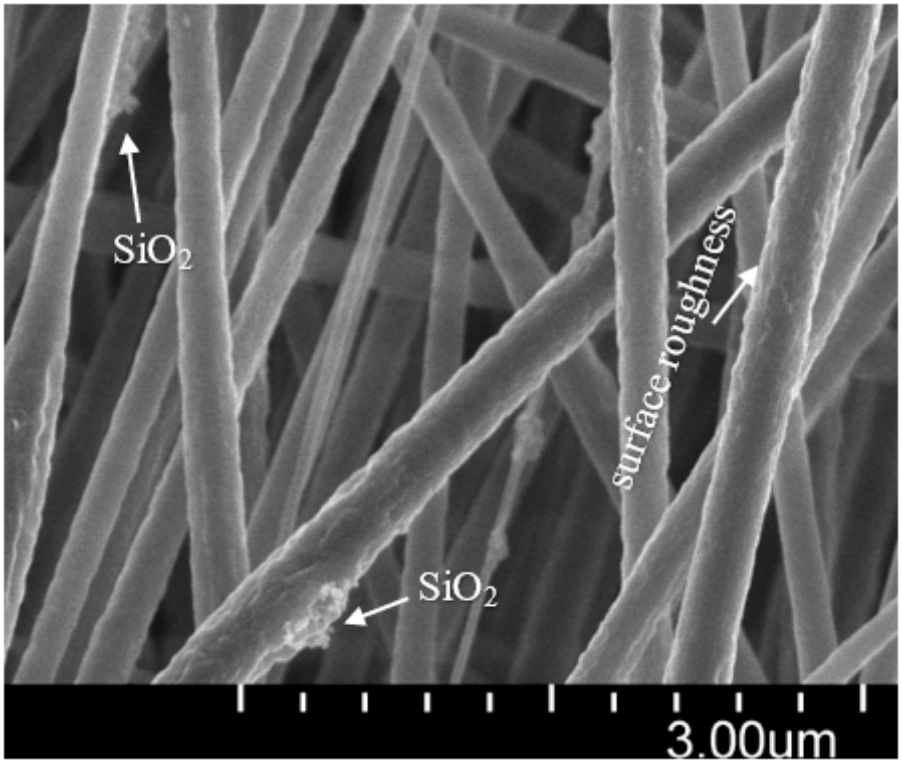


(**d**)

Figure 5. *Cont.*



(**e**)



(**f**)

Figure 5. Camera and SEM images of the electrospun membranes: (**a**) membrane surface morphology; (**b**) PAN membrane cross-section; (**c**) PAN NF membrane; (**d**) MWCNT/PAN membrane NFs; (**e**) PAN-SiO_2 membrane NFs; (**f**) PAN-SiO_2 fiber surface.

Figure 5e shows the SEM image of a SiO_2-doped PAN nanofibers (NFs) of a nanocomposite membrane. The infusing of SiO_2 has raised the average diameter of the NFs compared to pure PAN NFs. Further, the infusing of SiO_2 has improved the surface roughness and the specific surface area of the NFs [47], which could promote the membranes' adsorption efficiency. The SEM images showed that the nanofibers were beadless, confirming

that the electrospinning process operated at the appropriate conditions. Moreover, the doped SiO_2 particles were trapped in grid-like NFs, which could be an active site for CO_2 absorption, as seen in Figure 5f. In addition, the functionalization of nanoparticles has improved the dispersion stability of SiO_2, which has improved the SiO_2 stability inside the doped nanofibers and thus produced stable nanocomposite membranes.

3.1.2. Thermogravimetric Analysis of the Membranes

To obtain the thermal degradation mechanism of PAN and PAN nanocomposite membranes, TGA and DTG analysis was carried out in a nitrogen environment and displayed in Figure 6. The TGA results (refer to Figure 6a) indicated the onset of nanofiber decomposition ($T_{-5wt\cdot\%}$), which started at 308 °C for PAN, 313 °C for PAN-SiO_2, and 319 °C for the PAN-MWCNT nanocomposites, and the slow thermal decomposition occurred at temperatures greater than 400 °C. The curves show that three stages of decomposition, such as cyclization, cross-linking, and dissolution, occurred for both PAN and the PAN nanocomposites. For PAN, the initial loss of weight up to 308 °C is due to the cyclization reaction of the polymer [48], and the second stage of thermal degradation from 308 to 420 °C correlates to the chain dissolution of cyclized chains (polymer degradation) and unreacted polymer chains [48]. The last stage, at a temperature greater than 420 °C, corresponds to the gradual thermal decomposition that generates non-inflammable char residues. The PAN doped with MWCNTs and SiO_2 showed a similar degradation. The ($T_{-5wt.\%}$) loss of weight was used to estimate the initial thermal decomposition of polymer nanocomposites [49]. The addition of 7 wt.% functionalized GA-SiO_2 and 4 wt.% functionalized GA-MWCNTs increased the $T_{5\%}$ temperature of PAN 5 and 11 °C higher, respectively. Further, PAN-SiO_2 has shown a lower mass loss rate compared to PAN and PAN-MWCNT membranes, as shown in Figure 6b. This could be due to the varying influences with the addition of MWCNTs and SiO_2. Since the MWCNTs are good heat conductors, the higher wt.% might have promoted uniform heating, resulting in accelerated cyclization reactions. In some cases, the MWCNTs could act as catalysts for cyclization reactions, resulting in a higher loss of mass rate [50]. On the other hand, SiO_2 could act as a physical cross-linking agent, forming a more stable 3D network by reacting with the polymer chains. In addition, SiO_2 could act as a barrier, preventing the excessive thermal degradation of PAN during the cyclization process [51]. This might have resulted in a lower rate of mass loss for PAN-SiO_2 compared to PAN-MWCNT nanocomposite membranes. The decomposition temperature at the maximum rate (T_{peak}) (refer to Figure 6b) and the total weight loss of PAN and its nanocomposites are given in Table 1.

Table 1. Thermal analysis of pure PAN and PAN nanocomposite membranes.

Samples	$T_{-5wt\%}$ (°C)	T_{peak} (°C)	% Total Loss of Mass
PAN	308	360	75.2
PAN-MWCNTs (4 wt.%)	313	362	79
PAN-SiO_2 (7 wt.%)	319	344	71.7

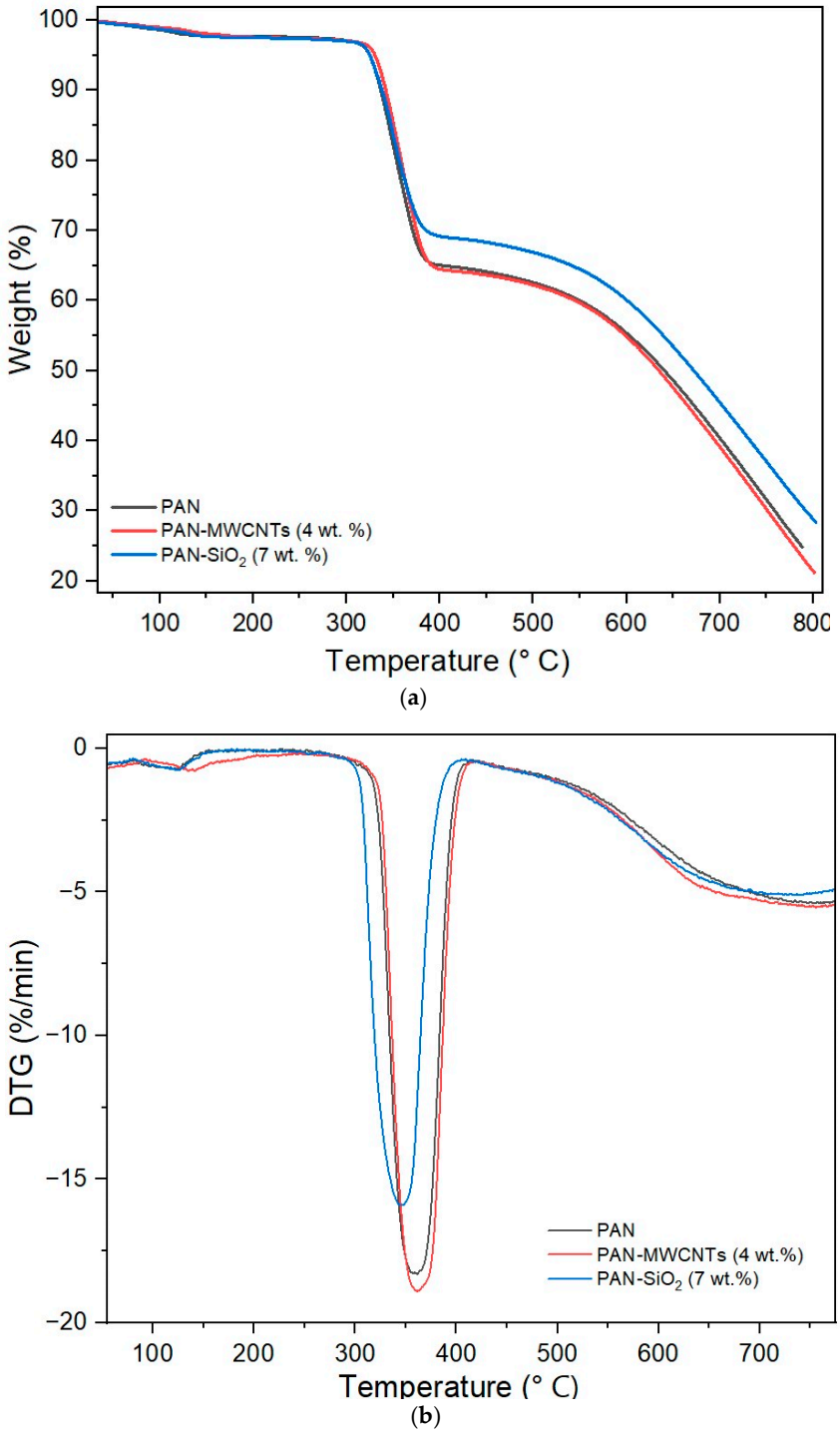


Figure 6. (**a**) TGA curves; (**b**) DTG curves of PAN and PAN nanocomposite membranes.

3.1.3. FTIR Analysis

The FTIR spectra for PAN, PAN with 7 wt.% of SiO_2, and 4 wt.% of MWCNTs are shown in Figure 7. The membranes were analyzed after exposure to the CO_2 separation process. The peaks with moderate intensity at 3600–3650 cm^{-1} correspond to the OH and NH_2 functional groups, demonstrating that the GA-functionalized nanoparticles are infused into PAN-SiO_2 and PAN-MWCNT membranes. The FTIR peaks at 2930 to 2970 cm^{-1} of the C-H stretching related to CH_2 groups of polyacrylonitrile structure. Though the MWCNTs and SiO_2 do not have significant C-H stretching vibration, adding MWCNTs and SiO_2 increased the peak intensity. The peak at 2245 cm^{-1} of the stretching of the nitrile group (-CN) [52], suggests that the PAN is the consistent component across all these

membranes [53]. The reaction between the GA-functionalized SiO_2 and MWCNTs with PAN could be seen in a peak at 1150 cm^{-1} for C-O stretching vibrations, which might be either due to the functionalization of the nanoparticles or due to the interactions between PAN and the functionalized nanoparticles [54,55]. Further, the peak at 950–960 cm^{-1} is commonly linked to the out-of-plane bending vibrations of C-H bonds in aromatic rings from the PAN component in the PAN-MWCNT membrane [56]. In the PAN-SiO_2 membrane, this peak can be accredited to the bending vibrations of Si-OH groups, indicating the occupancy of the hydroxyl group on the silica particles [57]. Following the analysis, it can be confirmed that the nanoparticles' functionalization helped improve the interactions with PAN polymer, which is expected to enhance the membrane CO_2 separation efficiencies.

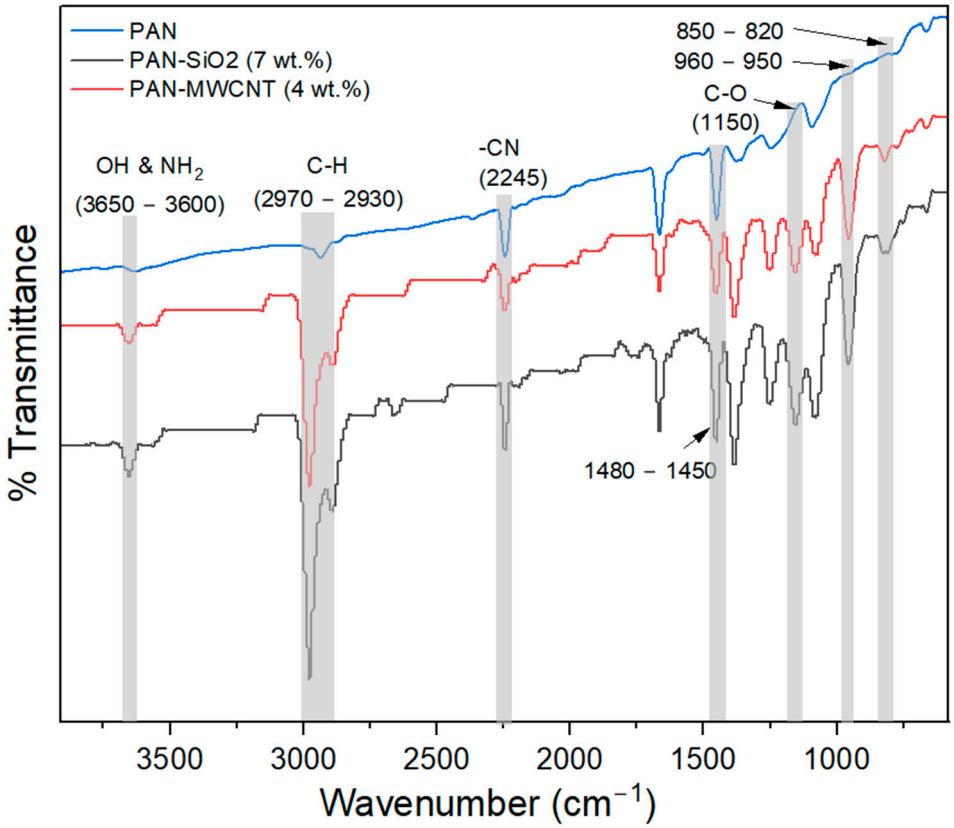


Figure 7. FTIR spectra of PAN, PAN-SiO_2, and PAN-MWCNT membrane.

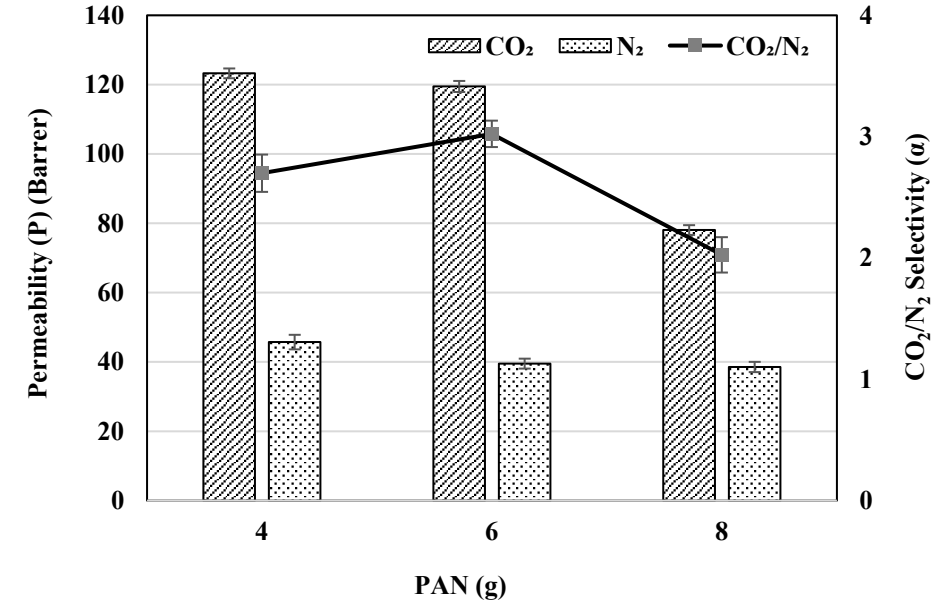
3.2. Membrane Performance

The performance of both PAN and the PAN nanocomposite membranes was determined using permeability, selectivity, diffusivity, and solubility.

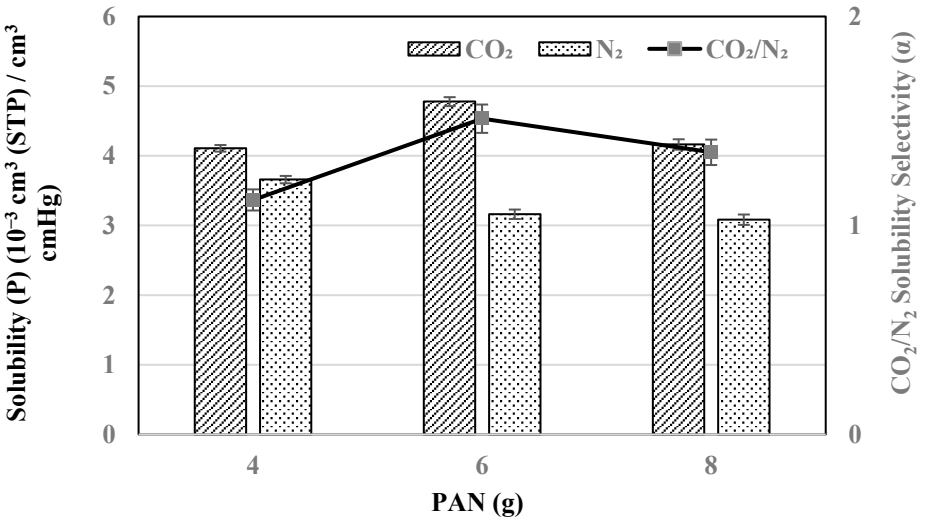
3.2.1. Pure PAN Membrane

Figure 8 shows the gas permeation properties of pure PAN membranes. As explained before, the pure PAN membranes with weight loadings of 4, 6, and 8 g of PAN were tested. By comparing the three different weight loadings, the PAN with a lower weight (4 g) has shown a higher permeability and selectivity than the PAN with 6 and 8 g of weight loadings, as displayed in Figure 8a. The highest CO_2 permeability (P_{CO2}) of 123 Barrer was obtained for 4 g of PAN, followed by 120 Barrer for 6 g of PAN, and the lowest P_{CO2} of 78 Barrer for 8 g of PAN. The reason behind the reduction in CO_2 permeability for increasing PAN concentrations could be due to the nanofibers overlapping and stacking (Figure 5a) along the membrane thickness (Figure 5b), which resulted in reduced free volume and increased tortuous transport pathway for CO_2 permeation [58]. On the other hand, no significant

change has been observed for N_2 gas permeation in all PAN weight loadings. PAN with 8 g weight loading has shown the least N_2 permeability (P_{N2}) of 38 Barrer, followed by 8 and 6 g with 39 and 46 Barrer, respectively. The lower P_{N2} for the increasing PAN weight fractions could be due to the N_2 higher kinematic diameter of 3.64 Å, compared to CO_2 with 3.3 Å [59], which would have resulted in lower N_2 permeation than CO_2.

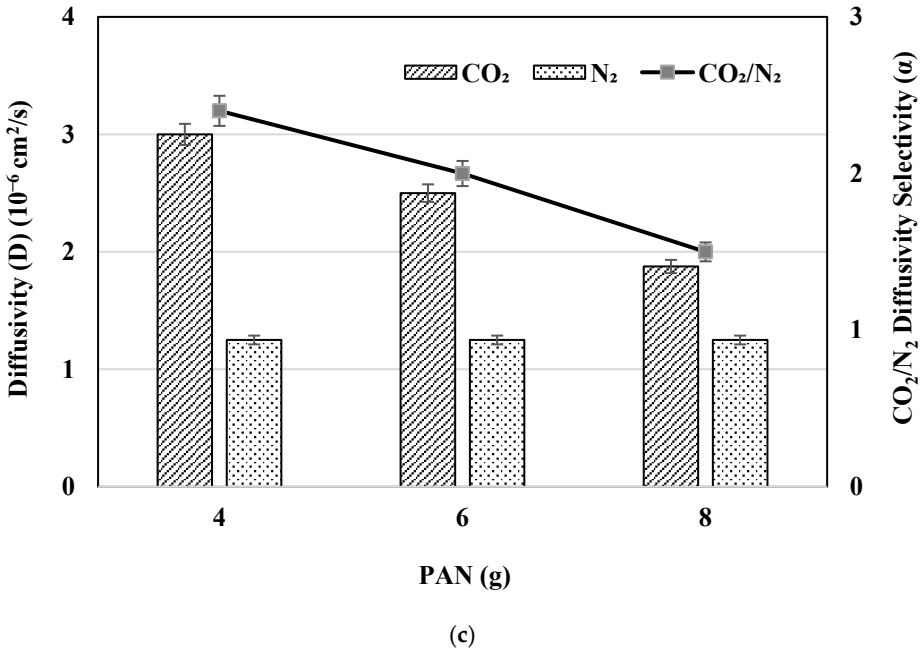


(**a**)



(**b**)

Figure 8. *Cont.*



(**c**)

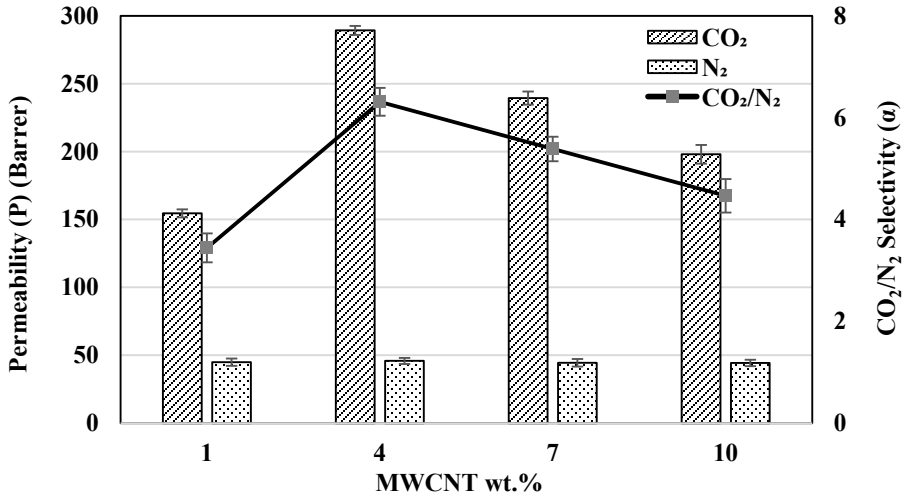
Figure 8. PAN membrane permeation results at different weight loadings: (**a**) permeability and selectivity; (**b**) solubility and solubility selectivity; (**c**) diffusivity and diffusivity selectivity.

The CO_2/N_2 selectivity ($\alpha_{CO2/N2}$) was calculated using the measured permeability and plotted in Figure 8a for three PAN weight loadings. Comparing all three PAN weight loadings, 6 g of PAN has the highest selectivity of 3, followed by 4 g and 8 g of PAN membrane with 2.7 and 2 selectivity, respectively. However, the solubility increases with the increase in PAN weight loading from 4 to 6 g, as shown in Figure 8b, and the diffusivity (refer to Figure 8c) showed a linear decrease with increased PAN weight loadings. This could be justified by the higher density of polymer fibers in a membrane for the increase in PAN weight fractions. The increased polymer density has enhanced the reaction between the gas and the PAN polymer chains, causing improved solubility. Fundamentally, the gas molecules are more likely to be absorbed by the polymer due to these stronger interactions. On the other hand, diffusivity decreases with increasing polymer fiber density due to reduced pathways/free volume for gases to pass across the membrane. The reduced free volume constricts the permeated gas to navigate through a tortuous pathway, which slows down their movement and thus results in lower diffusivity for the gas molecules.

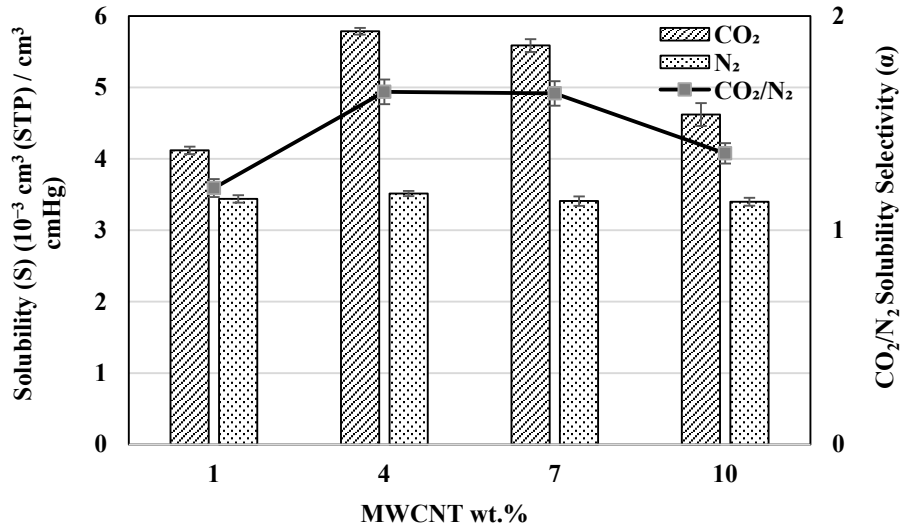
By comparing permeability, selectivity, and solubility, a PAN membrane with 6 g of PAN loading was selected as the suitable PAN weight fraction for the CO_2/N_2 separation. Thus, it was selected to manufacture MWCNTs and SiO_2-doped nanocomposite membranes with four weight fractions (1, 4, 7, and 10 wt.%) of the nanoparticles.

3.2.2. PAN-MWCNT Nanocomposite Membrane

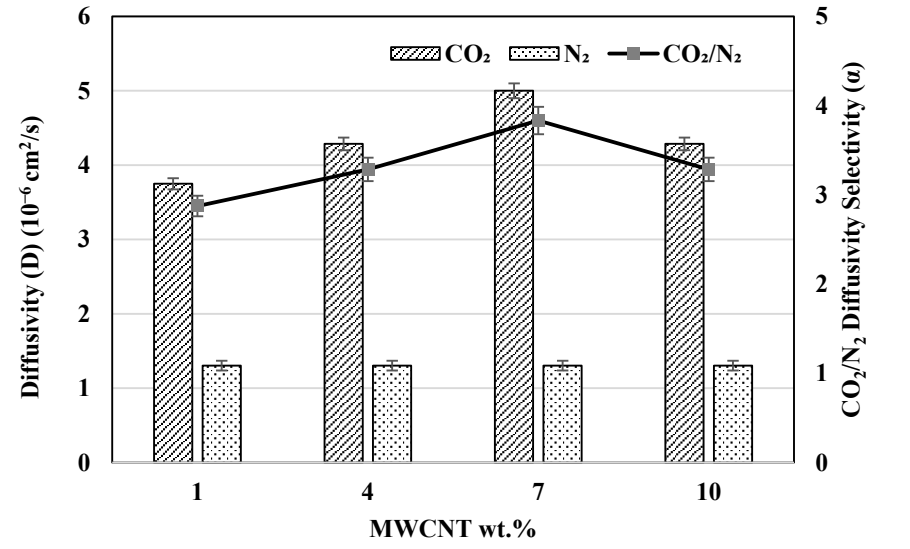
Figure 9 shows the permeability, selectivity, diffusivity, and solubility of 6 g of PAN doped with GA-functionalized MWCNT of 1, 4, 7, and 10 wt.% nanocomposite membrane, respectively. As the weight fractions of MWCNTs were increased, the CO_2 permeability increased further. Adding 4 wt.% of MWCNT shows the highest CO_2 permeability of 289 Barrer, followed by 7 and 10 wt.% with a permeability of 240 and 198 Barrer, respectively. However, the N_2 permeability did not show any appreciable increase as a result of the addition of MWCNTs and was in the range of 40–46 Barrer for all the MWCNT weight fractions. Consequently, the selectivity was measured and shown in Figure 9a. The results confirmed that MWCNTs with 4 wt.% have shown the highest selectivity of 6.3, followed by 5.4 and 4.5 for infusing 7 and 10 wt.% of MWCNT reinforcements, respectively.



(**a**)



(**b**)

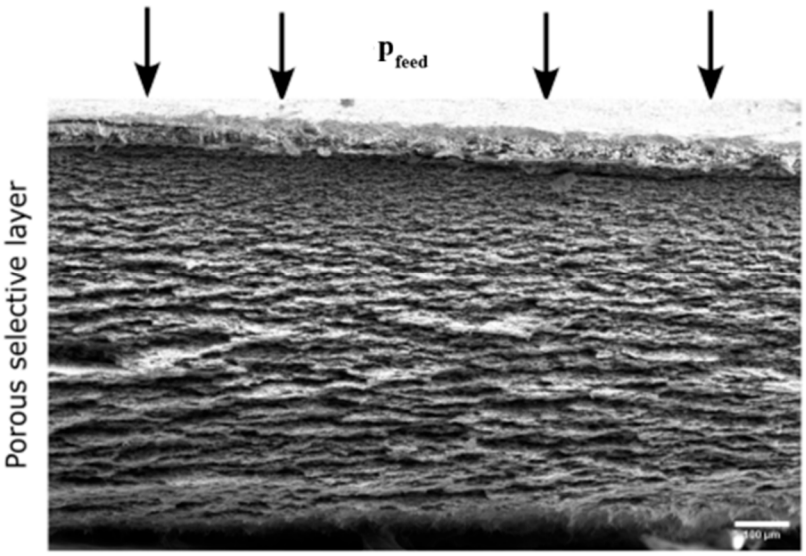


(**c**)

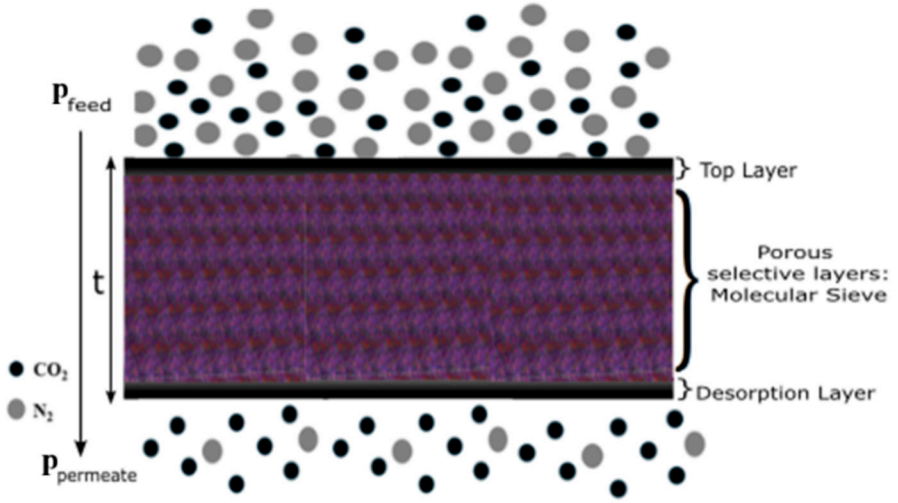
Figure 9. MWCNTs/PAN nanocomposite membrane permeation results at different weight fractions: (**a**) permeability and selectivity; (**b**) solubility and solubility selectivity; (**c**) diffusivity and diffusivity selectivity.

The rise in CO_2 permeability due to increased MWCNT loading from 1 to 4 wt.% could be due to the increased free volumes and porous pathways linked with the doping of MWCNTs with PAN polymer. The controlled addition of MWCNTs using electrospinning has formed flow channels within the membrane, which could have facilitated the transport of CO_2 molecules [60]. The continuous and smooth surface of the electrospun nanofibers has improved gas transport by providing low resistance to gas diffusion. This can be further confirmed by the well-aligned MWCNT-doped PAN nanofibers with smooth surfaces shown in Figure 5d, along with the porous selective layers shown in Figure 10a, which have resulted in CO_2 permeation within the dense MWCNT-doped nanofibers by the molecular sieve mechanism. Generally, the gas permeation across membranes is via solution–diffusion [61]. As such, doping the PAN polymer with MWCNTs controlled the porosity within the selective layers, which promoted the gas permeation process by the molecular sieve mechanism, as schematically illustrated in Figure 10b. Contingent to the solution–diffusion process, the gas is adsorbed at the selective layers before diffusing through the porous layers of the dense polymeric membrane by a molecular sieve mechanism. The CO_2 gas molecules selectively diffuse through the membrane while the larger gas molecules (N_2) retentate, and few diffuse. Further, the controlled porosity of adding the MWCNTs within the selective layers resulted in the CO_2 gas molecules diffusing through the molecular sieve mechanism. In contrast, the N_2 gas molecules with larger kinetic diameters were separated.

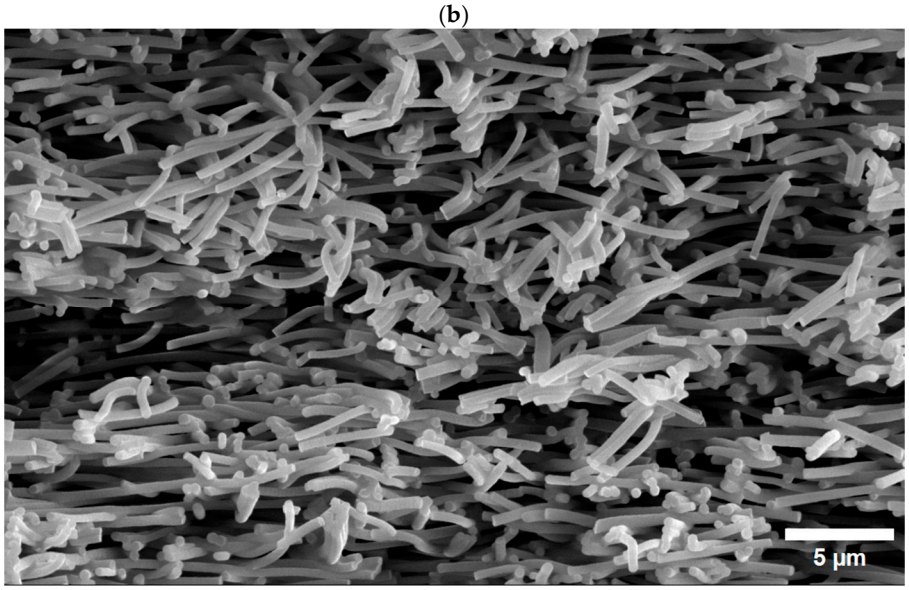
Additionally, increasing MWCNT nanoparticles can expand the free volume within the PAN matrix and disrupt its chains, providing more pathways for CO_2 molecule diffusion. Moreover, the size and shape of the pores in the membrane determine which molecules can pass through via the molecular sieve mechanism. Thus, adding MWCNT could have formed more uniform and well-defined pores that selectively permit CO_2 molecules to pass while blocking larger molecules. This might be a reasonable explanation for the enhanced CO_2 permeability and selectivity. Furthermore, Gum Arabic functionalization attached the OH functional group on the surface of the MWCNT, which has formed hydrogen bonding with the PAN. This bonding reaction developed an interfacial void between the nanoparticles and the PAN nanofiber. The interlinking voids could have helped to transport the gas molecules via the solution–diffusion mechanism. From the FTIR results in Figure 7, the stretching vibration (C-O) and aromatic C-H bending vibration were raised to higher waveforms due to CO_2 diffusion. The shifts can be accredited to the CO_2 interactions with the PAN-MWCNT nanocomposite membranes [62–64], which confirmed the solution–diffusion mechanism during the permeation process. The nitrile peak at 2245 cm^{-1} has altered due to the chemical reaction or physical adsorption of CO_2 with the PAN-MWCNT membranes, and the carbonate stretch peak at 1480–1450 cm^{-1} resulted from the CO_2 reaction with the PAN-MWCNT membrane. All these observations confirm that the solution–diffusion process is paramount in improving the permeation properties of the PAN-MWCNT nanocomposite membranes. However, after increasing MWCNT loadings above 4 wt.%, a decrease in CO_2 permeability has been observed due to more MWCNT nanoparticles occupying free volume spaces, decreasing gas transport pathways, as shown in Figure 10c. In the case of N_2 permeability, the increase in MWCNT weight fractions did not alter N_2 permeability significantly. As explained before, this might be due to their larger kinetic diameter of N_2 and an increase in fiber diameter for adding MWCNTs. Further, stalking and nanofiber overlapping could have also contributed to the lower P_{N2}, as discussed before. This has made CO_2 permeability the primary factor affecting the selectivity of the PAN-MWCNT nanocomposite for controlling the permeability and selectivity trade-off.



(**a**)



(**b**)



(**c**)

Figure 10. (**a**) SEM image of membrane cross-section; (**b**) a schematic of the solution–diffusion and molecular sieve mechanisms in a membrane separation; (**c**) PAN-MWCNT nanocomposite membrane nanofibers.

Similarly, the solubility and diffusivity were estimated from the experimental data and illustrated in Figure 9b,c. Since the solubility, diffusivity, and permeabilities are interlinked, the increase in solubility and diffusivity for adding MWCNTs from 1 to 4 wt.% is understandable. However, the increase in MWCNTs above 4 wt.% decreased the solubility and diffusivity. This could be because of the loss of polymer volume for adsorption due to the increasing weight fractions of MWCNTs. In addition, an increase in MWCNT weight fractions could have resulted in the agglomeration of the nanoparticles, which might have reduced gas transport pathways.

3.2.3. PAN-SiO_2 Nanocomposite Membrane

Figure 11 shows the permeability, selectivity, diffusivity, and solubility of PAN-SiO_2 nanocomposite membranes with the SiO_2 weight fractions of 1, 4, 7, and 10 wt.%. Figure 11a shows the permeability and selectivity of PAN-SiO_2 membranes. Similarly to MWCNTS, the permeability and selectivity have increased for the increase in SiO_2 weight fractions; as such, the highest increase in CO_2 permeability was noticed at 7 wt.% of SiO_2-doped PAN with the P_{CO2} of 325 Barrer, followed by 4, 1, and 10 wt.% with 233, 227, and 212 Barrer, respectively. The results indicated that CO_2 permeability was improved when SiO_2 wt.% loading increased from 1 to 7 wt.% of SiO_2, then started to decrease upon the addition of 10 wt.%. Similarly to the previous results, the addition of SiO_2 did not show a significant change in N_2 permeability, and the permeability was in the range of 44–48 Barrer for all the weight fractions. The CO_2/N_2 selectivity at 7 wt.% of SiO_2 had the best selectivity ratio of 7, followed by 1, 4, and 10 wt.% with 5.1, 5, and 4.5, respectively.

The increase in permeability and selectivity for the addition of SiO_2 could be attributed to the reaction mechanisms associated with hydrogen bonding [65] and the interlinking network between the SiO_2 particles and polymer chains due to functionalization [66]. Similarly to MWCNT utilization, Gum Arabic functionalization attached the OH functional group on the surface of the SiO_2, which has formed hydrogen bonding with the polymer chains that developed an interlinking void between the nanoparticles and the surrounding PAN within the nanofiber, which helped transport the gas molecules by the solution–diffusion mechanism. Moreover, the FTIR results shown in Figure 7 confirm that the nitrile peak at 2245 cm^{-1} has altered due to chemical reactions or the physical adsorption of CO_2 with PAN-SiO_2 membranes. The reaction of CO_2 with PAN-SiO_2 could be observed as a carbonate stretch at the 1450 cm^{-1} peak. These observations confirm that the infusing of SiO_2 increased the permeation properties of PAN-SiO_2 nanocomposite membranes. However, the increase in SiO_2 weight fraction beyond 7 wt.% has decreased the CO_2 permeability, which might be attributed to the reduction in free volume at higher SiO_2 weight fraction occupying the available space and also due to the agglomeration of SiO_2 nanoparticles reducing gas pathways, as seen in Figure 5f.

Further, solubility and diffusivity were obtained using the experimental data. Figure 11b shows an increasing CO_2 solubility for adding 7 wt.% of SiO_2 and starts to decline afterwards. Similarly to the PAN-MWCNT case, the solubility decline could be because of the loss of polymer volume for gas adsorption/absorption from the SiO_2 nanoparticles for the higher-weight fractions. This could also be attributed to an increase in nanoparticle agglomeration that reduced gas transport pathways. Figure 11c shows that CO_2 diffusivity has a positive linear relationship with increased SiO_2 nanoparticle weight fractions. Table 2 below summarizes the experimental results obtained for pristine PAN and synthesized nanocomposite membranes for CO_2/N_2 separation at different weight fractions of nanoparticles.

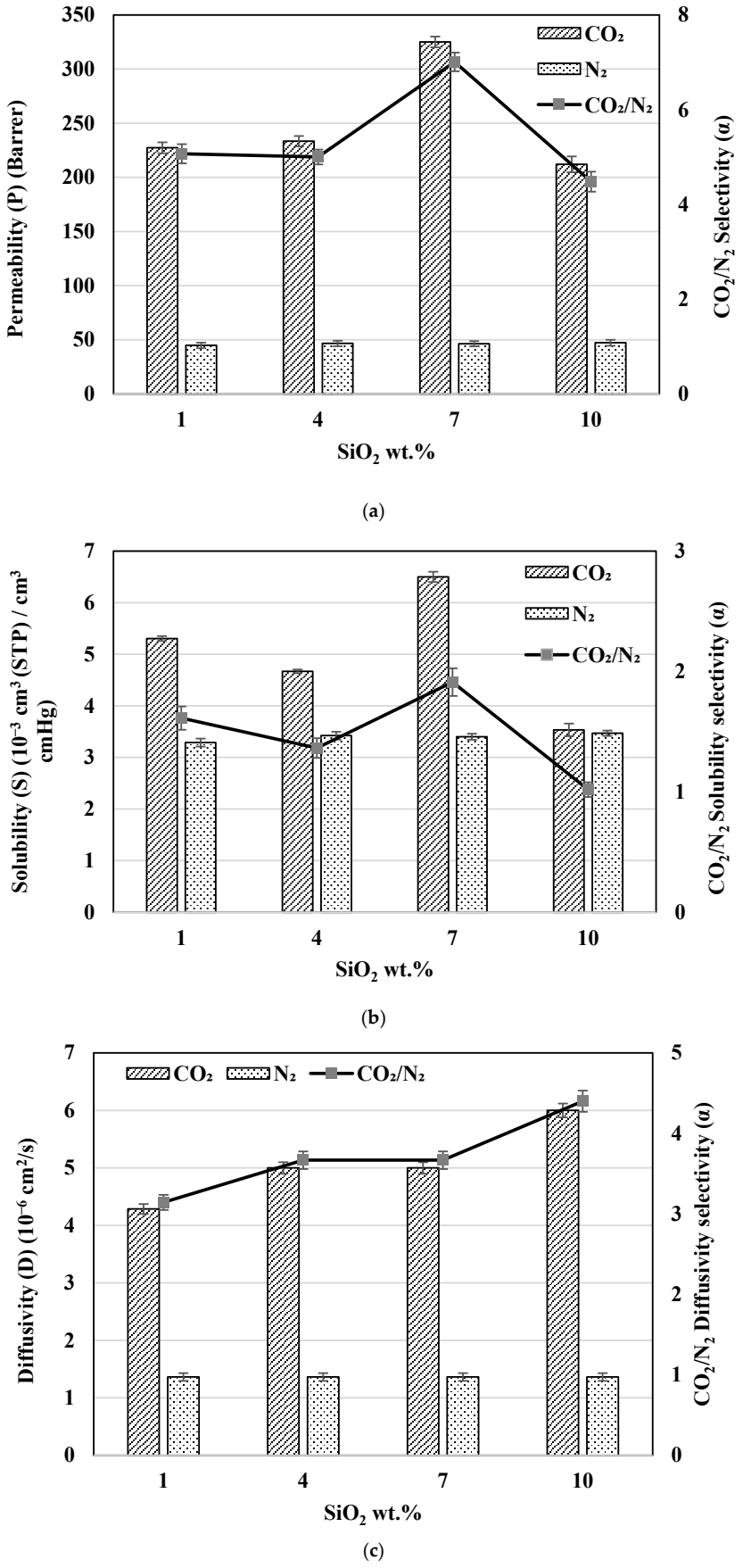


Figure 11. PAN-SiO_2 nanocomposite membrane permeation results at different weight fractions: (**a**) permeability and selectivity; (**b**) solubility and solubility selectivity; (**c**) diffusivity and diffusivity selectivity.

Table 2. Summary of the diffusion properties.

		Permeability		Selectivity	Diffusivity		Solubility		Selectivity	
		P_{CO2}	P_{N2}	$\alpha_{CO2/N2}$	D_{CO2}	D_{N2}	S_{CO2}	S_{N2}	α_D	α_S
		(Barrer)	(Barrer)		(10^{-6} cm^2/s)	(10^{-6} cm^2/s)	(10^{-3} cm^3 (STP)/cm^3 cmHg)	(10^{-3} cm^3 (STP)/cm^3 cmHg)		
PAN (g)	4	123.3	45.8	2.7	3.00	1.25	4.11	3.66	2.4	1.1
	6	119.5	39.5	3.0	2.50	1.25	4.78	3.16	2.0	1.5
	8	78.1	38.5	2	1.88	1.25	4.16	3.08	1.5	1.4
MWCNTs (wt.%)	1	154.5	44.9	3.4	3.75	1.30	4.12	3.44	2.9	1.2
	4	289.4	45.8	6.3	4.29	1.30	5.79	3.51	3.3	1.6
	7	239.5	44.5	5.4	5.00	1.30	5.59	3.41	3.8	1.6
	10	198.1	44.3	4.5	4.29	1.30	4.62	3.40	3.3	1.4
SiO_2 (wt.%)	1	227.3	44.8	5.1	4.29	1.36	5.30	3.29	3.1	1.6
	4	233.4	46.7	5.0	5.00	1.36	4.67	3.42	3.7	1.4
	7	325.0	46.4	7.0	5.00	1.36	6.50	3.40	3.7	1.9
	10	212.0	47.3	4.5	6.00	1.36	3.53	3.47	4.4	1.0

4. Validating the Experimental Results Using Analytical Modeling

We focused on validating the experimental results using the Effective Medium Analytical (EMA) model. The EMA approach was first adopted by Maxwell and used to estimate the electrical conductivity of the infused particles in a matrix. The EMA model was then extended to polymer nanocomposite with the assumption that a polymer matrix reinforced with nano-reinforcements can be substituted with an equivalent homogeneous material with the same composite properties [67–70]. Based on the assumption, Maxwell defined the effective permeability (P_{eff}) of a nanocomposite membrane [71] as given in Equation (5).

$$P_{eff} = P_M \left[\frac{P_{nf} + (n-1)P_M - (n-1)(P_M - P_{nf})\varphi_{nf}}{P_{nf} + (n-1)P_M + (P_M - P_{nf})\varphi_{nf}} \right] \quad (5)$$

P_M is the polymer matrix's permeability, P_{nf} is the nanofiller's permeability, φ_{nf} is the nanoparticle volume fraction within the range of $0 \leq \varphi_{nf} \leq 1$, and n is the nanoparticle shape factor. The Maxwell model has taken n = 3 for near-spherical fillers or spherical fillers, and hence, the effective permeability for spherical or near-spherical filers was written as

$$P_{eff} = P_M \left[\frac{P_{nf} + 2P_M - 2(P_M - P_{nf})\varphi_{nf}}{P_{nf} + 2P_M + (P_M - P_{nf})\varphi_{nf}} \right]$$

In the case of the solid spherical SiO_2 nanofillers, the P_{nf} of the nanoparticles is assumed to be 0 [70]; thus, the Maxwell equation becomes

$$P_{eff} = P_M \left[\frac{2(1 - 2\varphi_{nf})}{2 + \varphi_{nf}} \right] \quad (6)$$

However, the Maxwell model deviates significantly for the nanoparticles with tubular shape due to the difficulty in defining the shape factor (n). Hence, a modified Maxwell model was developed by Hamilton–Crosser [72], where the shape factor was defined as given below.

$$n = 3\psi^{-g}$$
$$\psi = 2\left(\tfrac{3}{4}\right)^{\frac{2}{3}} \frac{dL^2}{(d+2L)}$$

where

- ψ defines the sphericity of nanotubes.

- g is the empirical parameter and is taken as 1.
- d is the outer diameter of the tubular nanoparticles.
- L is the length of the tubular nanoparticles.

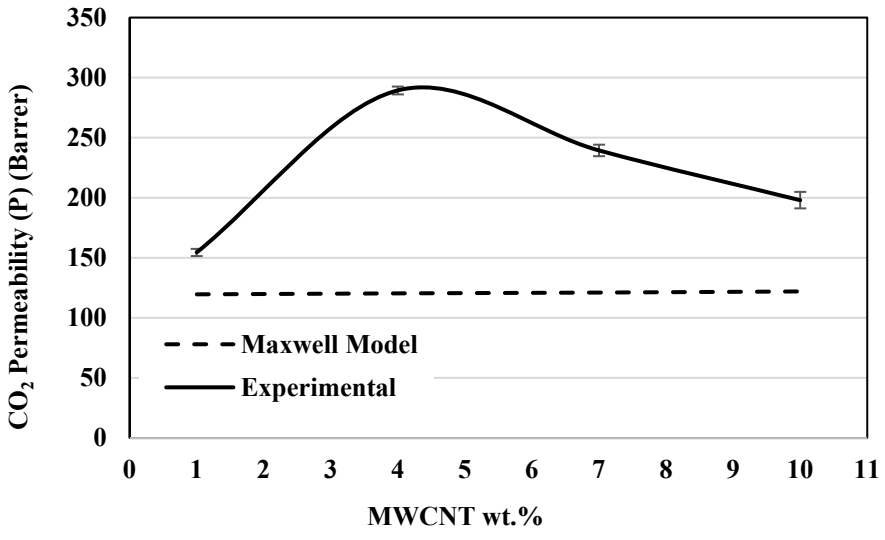
For the hollow tubular nanoparticles, the pores of MWCNTs are mesoporous, due to which the P_{nf} is assumed to be much larger than P_M, and thus, P_M and $(P_M - P_{nf})$ are neglected from the Maxwell equation and result in

$$P_{eff} = P_M\left[\frac{P_{nf}-(n-1)(-P_{nf})\varphi_{nf}}{P_{nf}+(-P_{nf})\varphi_{nf}}\right]$$
$$P_{eff} = P_M\left[\frac{P_{nf}+(n-1)(P_{nf})\varphi_{nf}}{P_{nf}(1-\varphi_{nf})}\right]$$

Further, using the MWCNT dimensions, the shape factor n = 0.34 was obtained and substituted into the above equation, which results in

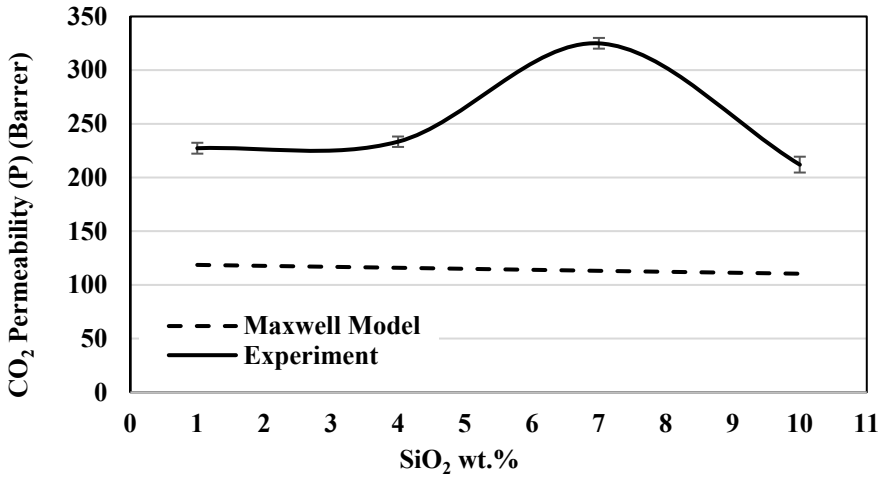
$$P_{eff} = \left[\frac{P_{nf}(1-0.66\varphi_{nf})}{P_{nf}(1-\varphi_{nf})}\right] \quad (7)$$

Using Equations (6) and (7), the Maxwell model permeability of spherical (SiO_2) and tubular (MWCNTs) nanocomposite membranes were determined and plotted with experimental results and are shown in Figure 12. As can be seen, the permeabilities for both MWCNTs and SiO_2 are greater than the Maxwell model, which confirms that the addition of nanoparticles improved the gas permeabilities by increasing gas pathways as discussed before. The increasing permeabilities could also be justified by the existence of voids between the nanoparticles and the polymer [73]. Further, the increasing free volumes and controlled porosities within the polymer caused by the infusing of nanoparticles might have disturbed the polymer chain packing [74]. As discussed before, this could have increased the gas adsorption and permeation. However, the experimental results showed that an increase in CO_2 permeability started to reduce beyond 4 wt.% for MWCNTs and 7 wt.% for SiO_2-doped polymer nanocomposite membranes. The loss of matrix-free volume available for the CO_2 solution–diffusion mechanism could explain the decreasing permeabilities at higher nanoparticle weight fractions. In addition, an increase in nanoparticle weight fractions could have resulted in the agglomeration of the nanoparticles, reducing gas transport pathways.



(**a**)

Figure 12. *Cont.*



(**b**)

Figure 12. CO_2 permeability of (**a**) PAN-MWCNTs; (**b**) PAN-SiO_2 nanocomposite membrane.

5. Comparison with Other Studies

Table 3 shows the comparative nanocomposite membrane separation performance of the presented research works with results obtained from the literature. The comparison was mainly focused on PAN-based nanocomposite membranes and other semicrystalline polymers infused with MWCNTs and SiO_2 nanoparticles fillers. It clearly demonstrates that infusing MWCNTs and SiO_2 nanoparticles into the polymer matrix enhances CO_2 permeability but reduces CO_2/N_2 selectivity due to the permeability–selectivity trade-off relationship. Moreover, the nanocomposite membranes of PAN polymer with MWCNTs and SiO_2 have shown better CO_2 permeability than other combinations. However, the selectivity still needs improvement to achieve better membrane separation performance.

Table 3. Comparison with other studies.

Polymer	NPs	Feed Pressure (cmhg)	Temperature (K)	NPs (wt.%)	P_{CO2} (Barrer)	$\alpha_{CO2/N2}$	
PAN-Polyethylene oxide	Zeolitic imidazolate framework	225	298.15	0	100	80	[75]
				16.6	200	68	
PAN-Polysulfones	Iron oxide (black)	750	303.15	0	1.17	4.25	[76]
				5	2.14	4.52	
				10	2.53	4.73	
				15	3.19	3.78	
				20	3.81	3.49	
Polyethersulfone	MWCNTs	150	298.15	0	2.6	21	[77]
				1	3.2	23	
				3	3.5	21	
				5	4.5	22	
				10	3.5	18	
Pebax-1657	MWCNTs	225	298.15	0	60	30	[78]
				2.5	90	72	
				5	150.51	82.06	
				7.5	110	64	

Table 3. *Cont.*

Polymer	NPs	Feed Pressure (cmhg)	Temperature (K)	NPs (wt.%)	P_{CO2} (Barrer)	$\alpha_{CO2/N2}$	
Polyurethane	SiO_2	750	298.15	0	79.81	29.34	[79]
				5	75.98	30.27	
				10	73	33.49	
				15	68.9	38.49	
Pebax-Polyethylenimine	SiO_2	150	298.15	0	11.1	28.28	[80]
				5	17.67	11.34	
				10	19.83	9.88	
				20	20.58	9.76	
PAN	MWCNTs	76	308	0	119.50	3	This work
				1	154.50	3.4	
				4	289.40	6.3	
				7	239.50	5.4	
				10	198.10	4.5	
PAN	SiO_2	76	308	0	119.50	3	This work
				1	227.30	5.1	
				4	233.40	5	
				7	325.00	7	
				10	212.00	4.5	

6. Conclusions

This work developed novel nanocomposite membranes for CO_2/N_2 separation using electrospinning with Gum Arabic (GA)-functionalized MWCNT and SiO_2 nanoparticles doped with PAN polymer. Characterization tests (FTIR, SEM, TGA) showed that the GA functional group enhanced nanoparticle dispersion and prevented agglomeration, improving gas separation performance. SEM images revealed beadless membranes with well-distributed nanoparticles and smooth, defect-free fibers. The doped nanoparticles created continuous gas pathways, enhancing CO_2 permeability. MWCNT doping improved the mechanical and thermal properties, while SiO_2 doping increased fiber diameter, surface roughness, and specific surface area, boosting gas sorption and CO_2 permeation.

The gas separation results indicated that CO_2 permeability decreases with increasing PAN weight fractions for pure PAN membranes; this was due to denser nanofibers creating tortuous pathways, similarly affecting N_2 permeability. However, CO_2/N_2 selectivity initially improved with increased PAN weight but then declined due to lower CO_2 permeability. The best CO_2 permeability (119.5 Barrer) and CO_2/N_2 selectivity (3) were achieved with membranes containing 6 g of PAN. Additionally, PAN membranes showed an inverse relationship between solubility and diffusivity, and a direct relationship between diffusivity and permeability with increasing PAN weight fractions. The PAN-MWCNT nanocomposite membrane showed enhanced CO_2 permeability with increasing nanoparticle weight fractions, but selectivity decreased above 4 wt.% MWCNTs. The highest CO_2 permeability and CO_2/N_2 selectivity were 289.4 Barrer and 6.3, respectively, due to increased free volumes and porous pathways from the doped MWCNTs. The N_2 permeability did not increase significantly due to larger kinetic diameter and increased fiber diameter. The CO_2 solubility–permeability relationship suggested that higher MWCNT weight fractions improved CO_2 solubility in the pure PAN membrane, contributing to increased CO_2 permeability. The gas separation for PAN-SiO_2 nanocomposite membranes improved CO_2 permeability with increasing SiO_2 weight fractions, but selectivity declined above

7 wt.% of SiO_2. At 7 wt.% SiO_2, the membrane achieved a CO_2 permeability of 325 Barrer and CO_2/N_2 selectivity of 7. GA functionalization improved permeability and selectivity through hydrogen bonding and interlinking networks between SiO_2 and PAN chains. FTIR confirmed these observations. Solubility and diffusivity analyses showed increased CO_2 solubility up to 7 wt.%, after which it declined. CO_2 diffusivity had a positive relationship with permeability, suggesting that increased SiO_2 reinforcement enhanced CO_2 diffusivity, boosting CO_2 permeability. The experimental results were compared with the Maxwell model. The experimental permeabilities for both MWCNTs and SiO_2 were greater than the Maxwell model, which confirmed that the addition of nanoparticles had an impact on the gas permeabilities due to the increasing gas pathways, as discussed before.

Author Contributions: All authors contributed to the research conception, experimental design, and data processing. Material preparation, experiments, and data collection were performed by D.A. The manuscript and discussion were written by D.A. and J.M. Supervised by J.M. All authors have read and agreed to the published version of the manuscript.

Funding: The partial financial support by the Natural Sciences and Engineering Research Council of Canada (NSERC DDG-2020-00046) and the Vice-President (Research) Discretionary Fund at the University of Regina are gratefully acknowledged. The views expressed herein are those of the writers and not necessarily of the research and funding partners.

Data Availability Statement: Data were included in the manuscript.

Conflicts of Interest: The authors declare that they have no conflict of interest.

References

1. Dong, L.; Huang, Z. Some Evidence and New Insights for Feedback Loops of Human-Nature Interactions from a Holistic Earth Perspective. *J. Clean. Prod.* **2023**, *432*, 139667. [CrossRef]
2. McGlade, C.; Ekins, P. The Geographical Distribution of Fossil Fuels Unused When Limiting Global Warming to 2 °C. *Nature* **2015**, *517*, 187–190. [CrossRef]
3. Baer, H. *Global Warming and the Political Ecology of Health*; Routledge: London, UK, 2016; ISBN 9781315428017.
4. Nemethova, H.; Petricek, P.; Zgodavova, Z.; Tobisova, A.; Vagner, J.; Choma, L. Civil Aviation Experience for the Air Force: The Impact of Global Climate Change on the Selected Parameters of the Cessna Citation XLS+. In Proceedings of the 2019 International Conference on Military Technologies (ICMT), Brno, Czech Republic, 30–31 May 2019; IEEE: New York, NY, USA, 2019; pp. 1–6.
5. Lee, J.W.; Kim, S.; Torres Pineda, I.; Kang, Y.T. Review of Nanoabsorbents for Capture Enhancement of CO_2 and Its Industrial Applications with Design Criteria. *Renew. Sustain. Energy Rev.* **2021**, *138*, 110524. [CrossRef]
6. Gür, T.M. Carbon Dioxide Emissions, Capture, Storage and Utilization: Review of Materials, Processes and Technologies. *Prog. Energy Combust. Sci.* **2022**, *89*, 100965. [CrossRef]
7. Biermann, M.; Normann, F.; Johnsson, F.; Hoballah, R.; Onarheim, K. Capture of CO_2 from Steam Reformer Flue Gases Using Monoethanolamine: Pilot Plant Validation and Process Design for Partial Capture. *Ind. Eng. Chem. Res.* **2022**, *61*, 14305–14323. [CrossRef]
8. Zhang, X.; Song, Z.; Gani, R.; Zhou, T. Comparative Economic Analysis of Physical, Chemical, and Hybrid Absorption Processes for Carbon Capture. *Ind. Eng. Chem. Res.* **2020**, *59*, 2005–2012. [CrossRef]
9. Kim, J.H.; Ha, S.Y.; Lee, Y.M. Gas Permeation of Poly(Amide-6-b-Ethylene Oxide) Copolymer. *J. Memb. Sci.* **2001**, *190*, 179–193. [CrossRef]
10. Ismail, A.F.; Chandra Khulbe, K.; Matsuura, T. *Gas Separation Membranes*; Springer International Publishing: Cham, Switzerland, 2015; ISBN 978-3-319-01094-6.
11. Richard Boyd and Grant Smith Semi-Crystalline Polymers. In *Polymer Dynamics and Relaxation*; Cambridge University Press: Cambridge, UK, 2007; pp. 199–226.
12. Jankowski, A.; Grabiec, E.; Nocoń-Szmajda, K.; Marcinkowski, A.; Janeczek, H.; Wolińska-Grabczyk, A. Polyimide-Based Membrane Materials for CO_2 Separation: A Comparison of Segmented and Aromatic (Co)Polyimides. *Membranes* **2021**, *11*, 274. [CrossRef] [PubMed]
13. Jiang, Y.; Zhang, B.; Zheng, Y.; Wu, Y. Highly Permselective Pebax/MWCNTs Mixed Matrix Membranes for CO_2/N_2 Separation. *Polym. Bull.* **2024**, *81*, 9699–9719. [CrossRef]

14. Robeson, L.M. The Upper Bound Revisited. *J. Memb. Sci.* **2008**, *320*, 390–400. [CrossRef]
15. Jana, A.; Modi, A. Recent Progress on Functional Polymeric Membranes for CO_2 Separation from Flue Gases: A Review. *Carbon. Capture Sci. Technol.* **2024**, *11*, 100204. [CrossRef]
16. Liu, M.; Seeger, A.; Guo, R. Cross-Linked Polymer Membranes for Energy-Efficient Gas Separation: Innovations and Perspectives. *Macromolecules* **2023**, *56*, 7230–7246. [CrossRef]
17. Lasseuguette, E.; Carta, M.; Brandani, S.; Ferrari, M.-C. Effect of Humidity and Flue Gas Impurities on CO_2 Permeation of a Polymer of Intrinsic Microporosity for Post-Combustion Capture. *Int. J. Greenh. Gas. Control* **2016**, *50*, 93–99. [CrossRef]
18. Kárászová, M.; Zach, B.; Petrusová, Z.; Červenka, V.; Bobák, M.; Šyc, M.; Izák, P. Post-Combustion Carbon Capture by Membrane Separation, Review. *Sep. Purif. Technol.* **2020**, *238*, 116448. [CrossRef]
19. Jin, H.; Xu, X. Preparation and Gas Separation of Amorphous Silicon Oxycarbide Membrane Supported on Silicon Nitride Membrane. *Membranes* **2024**, *14*, 63. [CrossRef]
20. Katare, A.; Kumar, S.; Kundu, S.; Sharma, S.; Kundu, L.M.; Mandal, B. Mixed Matrix Membranes for Carbon Capture and Sequestration: Challenges and Scope. *ACS Omega* **2023**, *8*, 17511–17522. [CrossRef] [PubMed]
21. De Angelis, M.G. Solubility of Gases in Membranes. In *Encyclopedia of Membranes*; Springer Berlin Heidelberg: Berlin/Heidelberg, Germany, 2014; pp. 1–3.
22. Kumar, R.; Mangalapuri, R.; Ahmadi, M.H.; Vo, D.-V.N.; Solanki, R.; Kumar, P. The Role of Nanotechnology on Post-Combustion CO_2 Absorption in Process Industries. *Int. J. Low-Carbon Technol.* **2020**, *15*, 361–367. [CrossRef]
23. Watson, J.C.; Pennisi, K.J.; Parrish, C.; Majumdar, S. Techno-Economic Process Optimization for a Range of Membrane Performances: What Provides Real Value for Point-Source Carbon Capture? *Carbon Capture Sci. Technol.* **2024**, *11*, 100182. [CrossRef]
24. Tseng, H.-H.; Kumar, I.A.; Weng, T.-H.; Lu, C.-Y.; Wey, M.-Y. Preparation and Characterization of Carbon Molecular Sieve Membranes for Gas Separation—The Effect of Incorporated Multi-Wall Carbon Nanotubes. *Desalination* **2009**, *240*, 40–45. [CrossRef]
25. Yagmur Goren, A.; Erdemir, D.; Dincer, I. Comprehensive Review and Assessment of Carbon Capturing Methods and Technologies: An Environmental Research. *Environ. Res.* **2024**, *240*, 117503. [CrossRef] [PubMed]
26. Secchi, E.; Marbach, S.; Niguès, A.; Stein, D.; Siria, A.; Bocquet, L. Massive Radius-Dependent Flow Slippage in Carbon Nanotubes. *Nature* **2016**, *537*, 210–213. [CrossRef] [PubMed]
27. Noy, A.; Park, H.G.; Fornasiero, F.; Holt, J.K.; Grigoropoulos, C.P.; Bakajin, O. Nanofluidics in Carbon Nanotubes. *Nano Today* **2007**, *2*, 22–29. [CrossRef]
28. Hu, C.-C.; Cheng, P.-H.; Chou, S.-C.; Lai, C.-L.; Huang, S.-H.; Tsai, H.-A.; Hung, W.-S.; Lee, K.-R. Separation Behavior of Amorphous Amino-Modified Silica Nanoparticle/Polyimide Mixed Matrix Membranes for Gas Separation. *J. Memb. Sci.* **2020**, *595*, 117542. [CrossRef]
29. Khalilinejad, I.; Kargari, A.; Sanaeepur, H. Preparation and Characterization of (Pebax 1657 + Silica Nanoparticle)/PVC Mixed Matrix Composite Membrane for CO_2/N_2 Separation. *Chem. Pap.* **2017**, *71*, 803–818. [CrossRef]
30. He, X. A Review of Material Development in the Field of Carbon Capture and the Application of Membrane-Based Processes in Power Plants and Energy-Intensive Industries. *Energy Sustain. Soc.* **2018**, *8*, 34. [CrossRef]
31. Zhao, Y.; Tian, H.; Ouyang, Y.; Xiang, A.; Luo, X.; Shi, X.; Ma, S. Poly (Vinyl Alcohol) Composite Membrane with Polyamidoamine Dendrimers for Efficient Separation of CO_2/H_2 and CO_2/N_2. *J. Polym. Environ.* **2022**, *30*, 4193–4200. [CrossRef]
32. Al-zharani, M.; Alyami, N.M.; Qurtam, A.A.; Aljarba, N.H.; Alkahtani, S.; Mubarak, M.; Daoush, W.M. Use of Multi-Walled Carbon Nanotubes (MWCNTs) Stabilized in Arabic Gum Colloidal Solution to Induce Genotoxicity and Apoptosis of Human Breast and Lung Cancer Cell Lines. *Front. Mater.* **2023**, *10*, 1229637. [CrossRef]
33. Bernal, Y.P.; Alvarado, J.; Juárez, R.L.; de Vasconcelos, E.A.; de Azevedo, W.M.; Soto-Cruz, B.-S. Synthesis and Characterization of Carbon Nanotubes/Silica Composites Using Gum Arabic. *Mater. Res. Express* **2018**, *5*, 075028. [CrossRef]
34. Boonprasertpoh, A.; Chantarangkul, P.; Thiangtham, S.; Kitiyanan, B.; Noisumdaeng, P.; Wootthikanokkhan, J.; Meeyoo, V. Fabrication and Characterizations of Electrospun Cellulose/CeO_2 Nanocomposite Membranes. *Cellulose* **2024**, *31*, 2957–2973. [CrossRef]
35. Nadaf, A.; Gupta, A.; Hasan, N.; Fauziya; Ahmad, S.; Kesharwani, P.; Ahmad, F.J. Recent Update on Electrospinning and Electrospun Nanofibers: Current Trends and Their Applications. *RSC Adv.* **2022**, *12*, 23808–23828. [CrossRef] [PubMed]
36. Ray, S.S.; Chen, S.-S.; Li, C.-W.; Nguyen, N.C.; Nguyen, H.T. A Comprehensive Review: Electrospinning Technique for Fabrication and Surface Modification of Membranes for Water Treatment Application. *RSC Adv.* **2016**, *6*, 85495–85514. [CrossRef]
37. Al-Abduljabbar, A.; Farooq, I. Electrospun Polymer Nanofibers: Processing, Properties, and Applications. *Polymers* **2022**, *15*, 65. [CrossRef]
38. Ahmadi Bonakdar, M.; Rodrigue, D. Electrospinning: Processes, Structures, and Materials. *Macromol* **2024**, *4*, 58–103. [CrossRef]
39. Varfolomeeva, L.A.; Skvortsov, I.Y.; Kuzin, M.S.; Kulichikhin, V.G. Silica-Filled Polyacrylonitrile Solutions: Rheology, Morphology, Coagulation, and Fiber Spinning. *Polymers* **2022**, *14*, 4548. [CrossRef] [PubMed]

40. Checchetto, R. Accurate Monitoring of Gas Mixture Transport Kinetics through Polymeric Membranes. *Sep. Purif. Technol.* **2021**, *277*, 119477. [CrossRef]
41. Dargahi, A.; Duncan, M.; Runka, J.; Hammami, A.; Naguib, H.E. Supercritical CO_2 Permeation in Polymeric Films: Design, Characterization, and Modeling. *Mater. Des.* **2023**, *227*, 111715. [CrossRef]
42. Gupta, Y.; Hellgardt, K.; Wakeman, R. Enhanced Permeability of Polyaniline Based Nano-Membranes for Gas Separation. *J. Memb. Sci.* **2006**, *282*, 60–70. [CrossRef]
43. Czichos, H.; Saito, T.; Smith, L. (Eds.) *Springer Handbook of Materials Measurement Methods*; Springer Berlin Heidelberg: Berlin/Heidelberg, Germany, 2006; ISBN 978-3-540-20785-6.
44. Lin, W.-H.; Vora, R.H.; Chung, T.-S. Gas Transport Properties of 6FDA-Durene/1,4-Phenylenediamine (PPDA) Copolyimides. *J. Polym. Sci. B Polym. Phys.* **2000**, *38*, 2703–2713. [CrossRef]
45. Ko, F.; Gogotsi, Y.; Ali, A.; Naguib, N.; Ye, H.; Yang, G.L.; Li, C.; Willis, P. Electrospinning of Continuous Carbon Nanotube-Filled Nanofiber Yarns. *Adv. Mater.* **2003**, *15*, 1161–1165. [CrossRef]
46. Kamran, U.; Park, S.-J. Chemically Modified Carbonaceous Adsorbents for Enhanced CO_2 Capture: A Review. *J. Clean. Prod.* **2021**, *290*, 125776. [CrossRef]
47. Ebrahimi, F.; Nabavi, S.R.; Omrani, A. Fabrication of Hydrophilic Hierarchical PAN/SiO_2 Nanofibers by Electrospray Assisted Electrospinning for Efficient Removal of Cationic Dyes. *Environ. Technol. Innov.* **2022**, *25*, 102258. [CrossRef]
48. Grassie, N.; McGuchan, R. Pyrolysis of Polyacrylonitrile and Related Polymers—I. Thermal Analysis of Polyacrylonitrile. *Eur. Polym. J.* **1970**, *6*, 1277–1291. [CrossRef]
49. Wu, S.-H.; Qin, X.-H. Effects of the Stabilization Temperature on the Structure and Properties of Polyacrylonitrile-Based Stabilized Electrospun Nanofiber Microyarns. *J. Therm. Anal. Calorim.* **2014**, *116*, 303–308. [CrossRef]
50. Yuan, S.; Bai, J.; Chua, C.K.; Wei, J.; Zhou, K. Highly Enhanced Thermal Conductivity of Thermoplastic Nanocomposites with a Low Mass Fraction of MWCNTs by a Facilitated Latex Approach. *Compos. Part A Appl. Sci. Manuf.* **2016**, *90*, 699–710. [CrossRef]
51. Giraldo, L.J.; Giraldo, M.A.; Llanos, S.; Maya, G.; Zabala, R.D.; Nassar, N.N.; Franco, C.A.; Alvarado, V.; Cortés, F.B. The Effects of SiO2 Nanoparticles on the Thermal Stability and Rheological Behavior of Hydrolyzed Polyacrylamide Based Polymeric Solutions. *J. Pet. Sci. Eng.* **2017**, *159*, 841–852. [CrossRef]
52. Farsani, R.E.; Raissi, S.; Shokuhfar, A.; Sedghi, A. FT-IR Study of Stabilized PAN Fibers for Fabrication of Carbon Fibers. *World Acad. Sci.* **2009**, *3*, 161–164.
53. Deng, S.; Yu, C.; Niu, J.; Liao, J.; Liu, X. Microwave Assisted Synthesis of Phosphorylated PAN Fiber for Highly Efficient and Enhanced Extraction of U(VI) Ions from Water. *Chem. Eng. J.* **2020**, *392*, 123815. [CrossRef]
54. Harandizadeh, A.H.; Aghamiri, S.; Hojjat, M.; Ranjbar-Mohammadi, M.; Talaie, M.R. Adsorption of Carbon Dioxide with Ni-MOF-74 and MWCNT Incorporated Poly Acrylonitrile Nanofibers. *Nanomaterials* **2022**, *12*, 412. [CrossRef] [PubMed]
55. Ying, Z.-Y.; Shao, Z.-D.; Wang, L.; Cheng, X.; Zheng, Y.-M. Sol–Gel SiO_2 on Electrospun Polyacrylonitrile Nanofiber for Efficient Oil-in-Water Emulsion Separation. *J. Mater. Sci.* **2020**, *55*, 16129–16142. [CrossRef]
56. Zhao, C.; Zhu, X.; Li, J.; Qi, W.; Zhao, Y.; Xu, K.; Yu, D.; Li, Y.; Zhou, J. Polyacrylonitrile/Multi-Walled Carbon Nanotubes/Polyurethane Electrospun Nanofiber Membranes for Sports Equipment. *Adv. Compos. Hybrid Mater.* **2024**, *7*, 44. [CrossRef]
57. Zemnukhova, L.A.; Panasenko, A.E.; Artem'yanov, A.P.; Tsoy, E.A. Dependence of porosity of amorphous silicon dioxide prepared from rice straw on plant variety. *BioResources* **2015**, *10*, 3713–3723. [CrossRef]
58. Sun, T.; Zheng, W.; Chen, J.; Dai, Y.; Li, X.; Ruan, X.; Yan, X.; He, G. Nanofibers Interpenetrating Network Mimicking "Reinforced-Concrete" to Construct Mechanically Robust Composite Membrane for Enhanced CO_2 Separation. *J. Memb. Sci.* **2021**, *639*, 119749. [CrossRef]
59. Talakesh, M.M.; Sadeghi, M.; Chenar, M.P.; Khosravi, A. Gas Separation Properties of Poly(Ethylene Glycol)/Poly(Tetramethylene Glycol) Based Polyurethane Membranes. *J. Memb. Sci.* **2012**, *415–416*, 469–477. [CrossRef]
60. Ahmad, M.; Tutuk, D.K.; Abdullah, B.; Ahmad, F.I. The Effect of Functionalization Carbon Nanotubes (CNTs) on the Performance of PES-CNTs Mixed Matrix Membrane. *Int. J. Sci. Eng.* **2010**, *1*, 15–20.
61. Sadeghi, M.; Chenar, M.P.; Rahimian, M.; Moradi, S.; Dehaghani, A.H.S. Gas Permeation Properties of Polyvinylchloride/Polyethyleneglycol Blend Membranes. *J. Appl. Polym. Sci.* **2008**, *110*, 1093–1098. [CrossRef]
62. Tan, T.L.; Lebron, G.B. Determination of Carbon Dioxide, Carbon Monoxide, and Methane Concentrations in Cigarette Smoke by Fourier Transform Infrared Spectroscopy. *J. Chem. Educ.* **2012**, *89*, 383–386. [CrossRef]
63. Nalawade, S.P.; Picchioni, F.; Marsman, J.H.; Janssen, L.P.B.M. The FT-IR Studies of the Interactions of CO_2 and Polymers Having Different Chain Groups. *J. Supercrit. Fluids* **2006**, *36*, 236–244. [CrossRef]
64. Maleh, M.S.; Kiani, S.; Raisi, A. Study on the Advantageous Effect of Nano-Clay and Polyurethane on Structure and CO_2 Separation Performance of Polyethersulfone Based Ternary Mixed Matrix Membranes. *Chem. Eng. Res. Des.* **2022**, *179*, 27–40. [CrossRef]

65. Zhuang, G.-L.; Tseng, H.-H.; Wey, M.-Y. Preparation of PPO-Silica Mixed Matrix Membranes by in-Situ Sol–Gel Method for H_2/CO_2 Separation. *Int. J. Hydrogen Energy* **2014**, *39*, 17178–17190. [CrossRef]
66. Hassanajili, S.; Khademi, M.; Keshavarz, P. Influence of Various Types of Silica Nanoparticles on Permeation Properties of Polyurethane/Silica Mixed Matrix Membranes. *J. Memb. Sci.* **2014**, *453*, 369–383. [CrossRef]
67. Pal, R. New Models for Thermal Conductivity of Particulate Composites. *J. Reinf. Plast. Compos.* **2007**, *26*, 643–651. [CrossRef]
68. Shah Buddin, M.M.H.; Ahmad, A.L. A Review on Metal-Organic Frameworks as Filler in Mixed Matrix Membrane: Recent Strategies to Surpass Upper Bound for CO_2 Separation. *J. CO2 Util.* **2021**, *51*, 101616. [CrossRef]
69. Monsalve-Bravo, G.M.; Bhatia, S.K. Modeling Permeation through Mixed-Matrix Membranes: A Review. *Processes* **2018**, *6*, 172. [CrossRef]
70. Myles, T.D.; Peracchio, A.A.; Chiu, W.K.S. Extension of Anisotropic Effective Medium Theory to Account for an Arbitrary Number of Inclusion Types. *J. Appl. Phys.* **2015**, *117*, 025101. [CrossRef]
71. Bouma, R.H.B.; Checchetti, A.; Chidichimo, G.; Drioli, E. Permeation through a Heterogeneous Membrane: The Effect of the Dispersed Phase. *J. Memb. Sci.* **1997**, *128*, 141–149. [CrossRef]
72. Shen, Y.; Lua, A.C. Theoretical and Experimental Studies on the Gas Transport Properties of Mixed Matrix Membranes Based on Polyvinylidene Fluoride. *AIChE J.* **2013**, *59*, 4715–4726. [CrossRef]
73. Ahn, J.; Chung, W.-J.; Pinnau, I.; Song, J.; Du, N.; Robertson, G.P.; Guiver, M.D. Gas Transport Behavior of Mixed-Matrix Membranes Composed of Silica Nanoparticles in a Polymer of Intrinsic Microporosity (PIM-1). *J. Memb. Sci.* **2010**, *346*, 280–287. [CrossRef]
74. Mahdavi, H.; Moradi-Garakani, F. Effect of Mixed Matrix Membranes Comprising a Novel Trinuclear Zinc MOF, Fumed Silica Nanoparticles and PES on CO_2/CH_4 Separation. *Chem. Eng. Res. Des.* **2017**, *125*, 156–165. [CrossRef]
75. Zheng, W.; Li, Z.; Sun, T.; Ruan, X.; Dai, Y.; Li, X.; Zhang, C.; He, G. PAN Electrospun Nanofiber Skeleton Induced MOFs Continuous Distribution in MMMs to Boost CO_2 Capture. *J. Memb. Sci.* **2022**, *650*, 120330. [CrossRef]
76. Homayoon, S.; Esfandiari, N. Gas Separation Properties of Polyacrylonitrile-Polysulfone-Iron Oxide Nanocomposite Membrane. *Sci. Iran.* **2020**, *27*, 1264–1274. [CrossRef]
77. Ge, L.; Zhu, Z.; Rudolph, V. Enhanced Gas Permeability by Fabricating Functionalized Multi-Walled Carbon Nanotubes and Polyethersulfone Nanocomposite Membrane. *Sep. Purif. Technol.* **2011**, *78*, 76–82. [CrossRef]
78. Wang, X.; Wang, Y.; Shan, Y.; Wang, X.; Yang, Y.; Zhang, F.; Chen, X. Polyethyleneimine-Modified Multi-Walled Carbon Nanotubes Mixed Matrix Membranes for CO_2/N_2 Separation. *J. Environ. Chem. Eng.* **2023**, *11*, 109537. [CrossRef]
79. Nematollahi, M.H.; Babaei, S.; Abedini, R. CO_2 Separation over Light Gases for Nano-Composite Membrane Comprising Modified Polyurethane with SiO_2 Nanoparticles. *Korean J. Chem. Eng.* **2019**, *36*, 763–779. [CrossRef]
80. Shafiee, M.; Akbari, A.; Bahreini pour, I.; Foroutan, R.; Ramavandi, B. The Permeability and Selectivity of Nanocomposite Membrane of PEBAx 1657/PEI/SiO_2 for Separation of CO_2, N_2, O_2, CH_4 Gases: A Data Set. *Data Brief* **2020**, *28*, 104800. [CrossRef]

Disclaimer/Publisher's Note: The statements, opinions and data contained in all publications are solely those of the individual author(s) and contributor(s) and not of MDPI and/or the editor(s). MDPI and/or the editor(s) disclaim responsibility for any injury to people or property resulting from any ideas, methods, instructions or products referred to in the content.